TECNOLOGIA SETÚBAL
ESCOLA SUPERIOR
POLITÉCNICO SETÚBAL

SAÚDE
ESCOLA SUPERIOR
POLITÉCNICO SETÚBAL

SARA BRUNO MARTINS

CORROSION AND FATIGUE BEHAVIOUR OF BIODEGRADABLE IRON SCAFFOLDS FOR BIOMEDICAL APPLICATIONS

Dissertation to obtain the Master of Science Degree in Biomedical Engineering

SUPERVISOR

Profª. Doctor Maria João Pedroso Carmezim,

Prof. Doctor Ricardo António Lamberto Duarte Claúdio.

December 2025

PRR Plano de Recuperação e Resiliência
REPÚBLICA PORTUGUESA
Financiado pela União Europeia NextGenerationEU

SARA BRUNO
MARTINS

CORROSION AND FATIGUE BEHAVIOUR OF BIODEGRADABLE IRON SCAFFOLDS FOR BIOMEDICAL APPLICATIONS

EXAMINATION COMMITTEE

Chairperson: Prof. Doctor Célio Gabriel Figueiredo Pina
Supervisor:
Prof. Doctor Ricardo António Lamberto Duarte Claúdio
Vogal: Prof. Doctor Luís Filipe Galrão dos Reis, IST/ ULisboa

December 2025

Just keep swimming!

Dory

Agradecimentos

Gostaria de expressar a minha sincera gratidão à minha orientadora, Professora Doutora Maria João Carmezim, pela orientação científica, dedicação e permanente disponibilidade demonstradas ao longo deste trabalho, bem como pelos ensinamentos, incentivo e apoio que foram determinantes para a concretização desta dissertação, no âmbito do projeto Gradimp-*Implantes biodegradáveis em ferro poroso obtidos por fabrico aditivo*, PTDC/CTM-CTM/3354/2021.

Expresso ainda a minha sincera gratidão ao meu orientador, Professor Doutor Ricardo Cláudio, pela orientação científica, disponibilidade e pelos conhecimentos transmitidos, que enriqueceram o desenvolvimento deste trabalho, bem como pelo apoio e incentivo prestados ao longo de todo o percurso.

Agradeço também à Escola Superior de Tecnologias de Setúbal, do Instituto Politécnico de Setúbal, pela oportunidade e pelas condições proporcionadas para a realização da dissertação, que representou uma etapa essencial no meu percurso académico e no meu desenvolvimento profissional.

Agradeço aos meus pais, pelo amor, paciência e apoio incondicional em todas as etapas deste percurso. Por acreditarem sempre em mim, mesmo quando eu duvidava, e por me ensinarem o valor do trabalho, da persistência e da humildade. Obrigada por estarem sempre ao meu lado, partilhando cada conquista e cada desafio, e por me darem tudo o que sou. É graças a vocês, e por vocês, que alcancei mais uma das minhas — e nossas — metas e sonhos. Obrigada por serem o exemplo que sempre segui e do qual me orgulho profundamente. Esta conquista é, acima de tudo, vossa.

Agradeço à minha irmã, que é a minha vida, o meu porto seguro e a minha melhor amiga. Obrigada por estares sempre presente, por me dares força nos dias difíceis e por celebrares comigo cada conquista como se fosse tua. Obrigada por seres o meu refúgio, e por me lembrares, sempre, quem eu sou. A tua presença é o meu conforto, e o teu amor, a minha maior inspiração. Nada teria o mesmo brilho sem ti — porque em cada passo que dou, levo comigo o teu amor, a tua força e o teu coração.

Agradeço ao meu namorado, aquele que traz luz, que nunca duvidou de mim e me fez acreditar que tudo é possível. Aquele que tem sempre a palavra certa, no momento certo. Pelo amor, pela paciência e pela compreensão. Obrigada por me dares calma quando o mundo parecia demasiado pesado, por acreditares em mim mesmo nas minhas maiores incertezas e por celebrares cada pequena conquista como se fosse tua. Obrigada por estares presente em cada passo. Hoje agradeço-te pelo que és, mas, sobretudo, pelo que me permitiste ser. Esta conquista é também tua.

Agradeço aos meus avós que partiram antes de me ver chegar aqui, cuja memória me acompanhou em cada etapa deste caminho. E à minha avó que me acompanha com o seu carinho e força.

Agradeço aos meus cães por serem a paz e o amor da minha vida.

Agradeço à Catarina Catalino, pela amizade, companheirismo e por ter sido a minha parceira incansável ao longo destes cinco maravilhosos anos. Agradeço profundamente toda a paciência (que, convenhamos, foi posta à prova mais vezes do que seria humanamente recomendável), o apoio incondicional e a boa disposição que nunca faltou, mesmo nos momentos de maior stress. Obrigada por estares presente em cada etapa — nas noites intermináveis de estudo, nas conversas, e em todas as gargalhadas que tornaram esta caminhada muito mais leve, divertida e inesquecível.

Agradeço ao Ruben Gomes, pelo apoio constante, amizade genuína e por ter sido uma das minhas maiores fontes de boa disposição ao longo deste percurso. Obrigada pelos momentos épicos e por me relembrares, nos dias mais difíceis, que também é importante saber abrandar.

Agradeço, com profunda gratidão, a todos os amigos que estiveram presentes ao longo desta caminhada. Pela companhia nos momentos de maior exigência, pelas palavras de incentivo, pela paciência nas ausências e pelas partilhas que trouxeram leveza aos dias mais intensos. Cada gesto, cada conversa e cada presença contribuíram para que este percurso fosse não apenas possível, mas também mais humano.

Resumo

A utilização de scaffolds biodegradáveis permite a regeneração progressiva do tecido ósseo enquanto se degrada de forma controlada, evitando custos e riscos com cirurgias pós-operatórias. Este estudo analisa o comportamento à corrosão, fadiga e fadiga-corrosão de scaffolds de ferro produzidos por manufatura aditiva, com células unitárias *Rhombitruncated Cuboctahedron* com 10% de densidade, que mimetizam o osso trabecular. Foram aplicadas técnicas como Espectroscopia de Impedância Eletroquímica, Microscópio eletrónico de varrimento, Microtomografia Computorizada, e Espectroscopia de Infravermelho por Transformada de Fourier, para analisar e caracterizar o comportamento à corrosão e mecânico dos scaffolds. Os ensaios de corrosão em fluido corporal simulado (SBF, 37ºC) revelaram a formação de uma película de óxidos, hidróxidos carbonatos e fosfatos na superfície do ferro. Nos ensaios de fadiga compressão-compressão, em SBF, verificou-se uma redução significativa da vida à fadiga dos scaffolds relativamente ao ambiente inerte. Embora a degradação à fadiga-corrosão seja elevada para scaffolders com 10% de densidade, a flexibilidade do processo de manufatura aditiva permite otimizar a densidade e melhorar o desempenho, contribuindo para o desenvolvimento de implantes biodegradáveis seguros e eficazes.

Palavras-chave: Manufatura Aditiva, Ferro, Corrosão, Fadiga, Fadiga-corrosão, Regeneração óssea.

Abstract

The use of biodegradable scaffolds allows for progressive bone tissue regeneration while degrading in a controlled manner, avoiding the costs and risks associated with post-operative surgery. This study analyses the corrosion, fatigue, and fatigue-corrosion behaviour of iron scaffolds produced by additive manufacturing, with Rhombitruncated Cuboctahedron unit cells with 10% density, which mimic trabecular bone. Techniques such as Electrochemical Impedance Spectroscopy, Scanning Electron Microscopy, Computed Microtomography, and Fourier Transform Infrared Spectroscopy were applied to analyse and characterize the corrosion and mechanical behaviour of the scaffolds. Corrosion tests in simulated body fluid (SBF, 37°C) revealed the formation of a film of oxides, hydroxides, carbonates, and phosphates on the iron surface. In compression-compression fatigue tests in SBF, a significant reduction in the fatigue life of the scaffolds was observed compared to the inert environment. Although fatigue-corrosion degradation is high for scaffolds with 10% density, the flexibility of the additive manufacturing process allows for density optimization and performance improvement, contributing to the development of safe and effective biodegradable implants.

Keywords: Additive Manufacturing, Iron, Corrosion, Fatigue, Corrosion-fatigue, Bone regeneration.

Table of Contents

List of Figures

List of Tables

List of Acronyms and Abbreviations

AM	Additive Manufacturing
ATR	Attenuated Total Reflectance
BMPs	Bone Morphogenetic Proteins
BR	Bone Regeneration
BTE	Bone Tissue Engineering
CE	Counter Electrode
DNA	Deoxyribonucleic Acid
EBM	Electron Beam Melted
EDS	Energy Dispersive Spectroscopy
EIS	Electrochemical Impedance Spectroscopy
HR	hot-rolled
FFT	Fast Fourier Transform
FTIR	Fourier Transform Infrared Spectroscopy
HR	Hot-rolled
PBF-LB	Laser Beam Powder Bed Fusion
Micro CT	Computed Microtomography
MPCs	Mesenchymal Progenitor Cells
m-SBF	Modified Simulated Body Fluid
OCP	Open Circuit Potential
OM	Optical Microscope
RBV	Reduced Build Volume

RE	Reference Electrode
RNA	Ribonucleic Acid
RTCO	Rhombitruncated cuboctahedron
SBF	Simulated Body Fluid
SCE	Saturated Calomel Electrode
SEM	Scanning Electron Microscopy
SLM	Selective Laser Melting
TGF-β	Transforming Growth Factor beta
VBA	Visual Basic for Applications
VEGF	Vascular Endothelial Growth Factor
WE	Working Electrode
3D	Three Dimension

List of Symbols

ε	Strain
ε_m	Accumulated mean strain during a fatigue cycle
ε_a	Strain amplitude during a fatigue cycle
$\Delta\varepsilon_m$	$\varepsilon_{initial} - \varepsilon_{final}$
θ	Phase angle
Z’	Real impedance
Z’’	Imaginarium impedance
|Z|	Impedance modulus
σ_y	Tensile yield strength
σ_{max}	Maximum normal stress
Ø	Diameter
°C	Degree Celsius
D	Diameter of the scaffold
E	Young’s modulus
E	Potential (mV vs SCE)
E_a	Amplitude of corrosion potential during a fatigue cycle (mV vs SCE)
E_m	Medium corrosion potential during a fatigue cycle
f	Frequency (Hz)
F_{amp}	Amplitude Force
F_{max}	Maximum Force
F_{med}	Medium Force

F_{min} Minimum Force

h_s height of the scaffold

log f Logarithmic Frequency

cm^{-1} Wavenumbers

R Load Ratio

Chapter 1

Introduction

The purpose of this chapter is to contextualize the central theme of this dissertation, establishing the scientific and technological motivation for the study, defining the research problem, and explaining the general objectives that guided the development of the work. A summary description of the structural organization of the thesis is also presented.

Motivation

This dissertation is motivated by the growing need to develop temporary and biodegradable medical solutions that combine adequate mechanical performance, controlled biodegradability, and compatibility with the clinical requirements of Bone Regeneration (BR). The aging population and the increased incidence of orthopaedic diseases, such as complex fractures, osteoporosis, or critical bone defects, have driven the search for effective alternatives to traditional bone grafts, which have limitations associated with availability, risk of rejection, infections, and morbidity at the donor site.

In this context, metal scaffolds produced by Additive Manufacturing (AM), specifically through the Laser Beam Powder Bed Fusion (PBF-LB) process as defined in ASTM 52900 (Additive Manufacturing-General Principles- ISO/ASTM 52900, 2021), stand out as a promising approach for orthopaedic applications. This method allows the fabrication of complex porous structures with high geometric precision, controlled porosity, and adjustable mechanical properties, which favour osseointegration and cell growth. The use of Fe as a biodegradable material has been gaining prominence due to its unique combination of mechanical strength, high ductility, and ability to degrade in vivo, eliminating the need for surgical removal of the implant after BR.

However, the behaviour of Fe in physiological environments under cyclic loading conditions remains poorly studied, with the interaction between corrosion and fatigue, known as fatigue corrosion behaviour —being one of the main challenges to overcome. This interaction can compromise the structural integrity of implants over time, especially considering that the degradation process is intentional and must be synchronized with the formation of new bone tissue. Therefore, it is essential to understand the failure mechanisms associated with corrosion fatigue to optimize the safety of biodegradable scaffolds.

This research aims to evaluate the fatigue-corrosion behaviour of porous Fe scaffolds produced by PBF-LB under conditions that simulate the physiological environment (SBF at 37 degree Celsius (°C)) and repeated mechanical loads. To this end, mechanical fatigue and corrosion tests, will be performed, both individually and in combination, in three-electrode cells with temperature control. The characterization of fractured surfaces by Scanning Electron Microscopy (SEM) and Energy Dispersive Spectroscopy (EDS), along with Computed Microtomography (Micro CT), will allow a detailed analysis of the failure mechanisms, both at the surface and internally.

Problem Statement

Increased life expectancy and the progressive aging of the world's population have led to a sharp increase in the incidence of orthopaedic conditions such as osteoporosis, fractures, subchondral defects, and bone tumours (Salari et al., 2021). As a result, bone has become the second most transplanted tissue worldwide, with approximately two million procedures performed annually (Laubach et al., 2024). The global bone transplant market is projected to grow, with estimates exceeding US$15 billion by 2031, highlighting the growing need for effective BR solutions (Global Bone Marrow Market, 2020).

However, current treatments have some limitations. One of the most promising solutions is the use of autograft, i.e. the patient's own tissue as a graft. However, this solution is limited by the size of the graft that can be harvested and carries potential risks such as limited availability and morbidity (Sohn & Oh, 2019) , risk of rejection and immunological complications (Łuczak et al., 2024), prolonged recovery time (Bayram et al., 2024) and pain (Lee et al., 2022).

This study aims to test under corrosion, fatigue and corrosion-fatigue customized scaffolds, capable of providing temporary mechanical support during BR and promoting osseointegration. These scaffolds would eliminate the need for additional surgeries to remove the implant, by integrating AM technologies with biodegradable metallic materials. This approach not only optimizes clinical outcomes in orthopaedic applications but also contributes to the advancement of regenerative medicine. It has the potential to positively impact quality of life and promote active ageing in populations.

Research Objectives

The main objective of this investigation is to evaluate the fatigue-corrosion behaviour of porous Fe metal scaffolds manufactured by PBF-LB under conditions that simulate the physiological environment including mechanical loading representative of human running. More specifically, the objectives of this work are as follows:

- Study high cycle fatigue behaviour in an inert environment (N_2 at 20 Hz) using fatigue compression-compression test;
- Evaluate the electrochemical performance of the scaffolds by conducting corrosion test, OCP and EIS, in a SBF solution at a temperature of 37°C;
- Investigate the combined behaviour of fatigue and corrosion in a physiological environment (SBF) at 4 Hz in a three-electrode cell with temperature control;
- Analyse fractured surfaces using SEM and EDS, as well as Micro CT to assess internal morphology and crack propagation, to understand the failure mechanisms involved;
- To establish a criterion for determining the end-of-life condition of porous Fe scaffolds under fatigue compression–compression.

This dissertation aims to deepen knowledge of the mechanical and corrosive durability of Fe scaffolds for use in BR. This will contribute to the advancement of biodegradable metallic biomaterials and the development of safer and more effective implants in orthopaedic clinical contexts.

Dissertation Organization

This dissertation is structured into six chapters, organized in a logical order that follows the development of the research. Chapter 1 introduces the scientific context of the work by presenting the motivation, general and specific objectives, and the problem framework. It also describes the document's overall structure, providing a foundation for understanding the topics covered.

Chapter 2 brings together relevant literature on BR and biodegradable scaffolds, Fe as a biomaterial. Its mechanical properties, corrosion and fatigue behaviour are discussed, as well as AM technologies applied to its production.

Chapter 3 describes the materials used and the experimental methods adopted. It covers mechanical, electrochemical, and morphological characterization tests. The methodologies applied to analyse fatigue-corrosion behaviour are highlighted, including tests in physiological media, SEM, EDS, Fourier Transform Infrared Spectroscopy (FTIR) and Micro CT.

Chapter 4 is dedicated to presenting the experimental results obtained throughout the study. It examines the responses of the Fe scaffolds in terms of mechanical strength and fatigue-corrosion behaviour, correlating the microstructural data with the functional performance in SBF.

Chapter 5 provides a critical analysis of the experimental results, focusing on the degradation behaviour of Fe structures subjected to cyclic loading in SBF. The analysis aims to determine the influence of the mechanical and corrosive environment, which mimics daily functional requirements, on the gradual degradation of the structure. The discussion seeks to establish whether the structure retains adequate structural integrity throughout the BR process, degrading only as new tissue forms. In this context, the results are evaluated in terms of their clinical relevance specifically, the balance between mechanical support and controlled biodegradation which is essential for temporary implants.

Chapter 6 summarizes the key findings of the study, emphasizing the scientific contributions gained from studying the mechanical and corrosive behaviour of Fe scaffolds produced by AM. Additionally, it outlines future research directions.

Chapter 2

Literature Review

This chapter surveys the literature relevant to AM Fe scaffolds, focusing on mechanical behaviour, and degradation, covering corrosion and corrosion-fatigue mechanisms in SBF and inert environments.

2.1. Bone Regeneration – Process and Scaffold Requirements

BR progresses through four sequential phases, as illustrated in Figure 2.1 a) hematoma formation and initial inflammation, b) development of a fibrocartilaginous callus with neovascularization, c) formation of a bony callus composed of spongy bone, and d) bone remodelling leading to structural consolidation and restoration. In critical-sized defects, a porous scaffold is implanted to support tissue regeneration by promoting cell adhesion, vascularization, and matrix deposition. (Łuczak et al., 2024; Percival et al., 2024; Shen et al., 2025; Toosi et al., 2023).

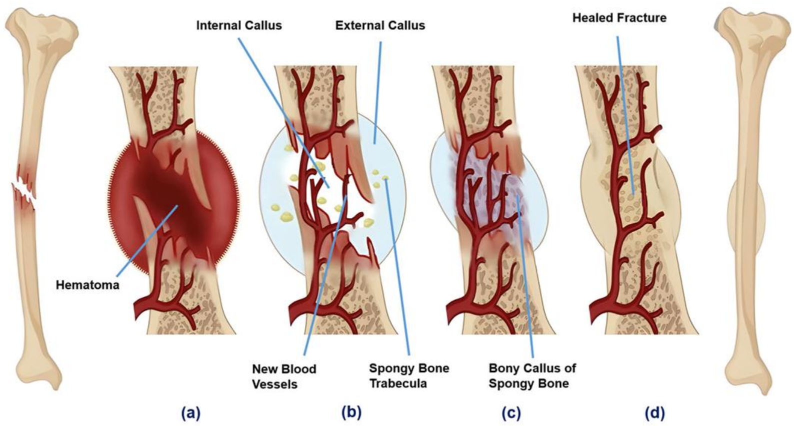

Figure 2.1 - Four stages of fracture repair (extracted from (Percival et al., 2024)).

An ideal scaffold for BR it should be degrading gradually at a controlled rate to match new bone formation (Tabrizian et al., 2024).

The scaffold must present an interconnected porous network that enables nutrient transport and tissue ingrowth. Pore size plays a critical role in mechanical and biological performance: macropores between 100 and 400 μm are generally considered optimal for BR, while smaller pores (<100 μm) limit tissue infiltration. Micropores (<10 μm) increase surface area and enhance early integration of the scaffold (Feng et al., 2023; Mukasheva et al., 2024; Yang et al., 2023).

The fracture toughness, compressive strength and Young's modulus (*E*) of cortical bone are between 2 and 12 MPa.m$^{1/2}$, 100-180 MPa and 7-30 GPa, respectively, while those of cancellous bone are between 0.1-0.8 MPa.m$^{1/2}$, 2-12 MPa and 0.2-0.5 GPa, respectively. Moreover, bone implants must have mechanical properties like those of natural bones to provide the necessary mechanical support to the defect site and the newly formed tissue during the bone repair process (Rezapourian et al., 2022).

Conventional metals such as titanium alloys offer high strength and biocompatibility but their high stiffness can induce stress shielding, reducing bone stimulation and long-term osseointegration (Francis et al., 2023; Jang et al., 2023; Schulze et al., 2023).

Among biodegradable metals, Fe has been explored for applications in BTE due to its favourable mechanical properties, including high strength and ductility (Percival et al., 2024). Its abundance and low cost make it an attractive biomaterial for biomedical scaffolds (Percival et al., 2024). However, poor osseointegration and possible mechanical mismatch between Fe and bone tissue are barriers to its widespread use (Ramaglia Amadasi et al., 2025). The in vivo performance of biodegradable porous Fe scaffolds has already been evaluated in large animal models. A one-year observational study compared 3D-printed porous Fe and Ti interference screws in a porcine anterior cruciate ligament reconstruction model. The Fe screws demonstrated progressive degradation, osteointegration, and mechanical stability over time, confirming their potential as bioactive, load-bearing implants for orthopaedic applications (Liu et al., 2025).

Biodegradable polymers such as PLA and PCL are widely used in scaffolds but lack the mechanical strength required for load-bearing applications(Kalva et al., 2025).

Ceramics such as HA and TCP are favoured for their osteoconductive, which promotes adhesion and bone cell growth. The similarity of these ceramics to the mineral component of bone makes them ideal for improving BR. However, their fragility may limit their use in areas of high mechanical stress. Integration with other materials, such as polymers, can help overcome these limitations by combining strength and bioactivity.

Fe has high ductility compared to Mg and Zn. In addition to its promising tensile yield strength (σ_y) and tensile strength, it also exhibits favourable ductility, and these properties impart high toughness to Fe-based materials. The relatively high ductility of Fe facilitates the design of topologically ordered structures for Fe-based frameworks, as it can withstand more extensive plastic deformation before fracture. High ductility also leads to high conformability and ease of forming more complex designs. This increases its potential to be excellently produced by AM techniques with more intricate and sophisticated architectures to meet the requirements of bone scaffolds (Bahrudin et al., 2025).

Recent studies on porous Fe-based scaffolds fabricated by AM, the designs are primarily based on cubic and diamond unit cells. The cubic unit cell, being the simplest, is likely the easiest to fabricate using AM processes. Despite its simplicity, its design has been shown to have the desired porosity range of natural bone, which is conducive to bone tissue growth. In addition, the uniform stress distribution in each connecting rod without sharp peaks is one of the main advantages of the cubic unit cell (Bahrudin et al., 2025).

The graph in Figure 2.2 clearly shows how corrosion and Fe degradation directly affect the mechanical properties of the material, which is critical for its use as biodegradable implant material (Y. Li et al., 2018).

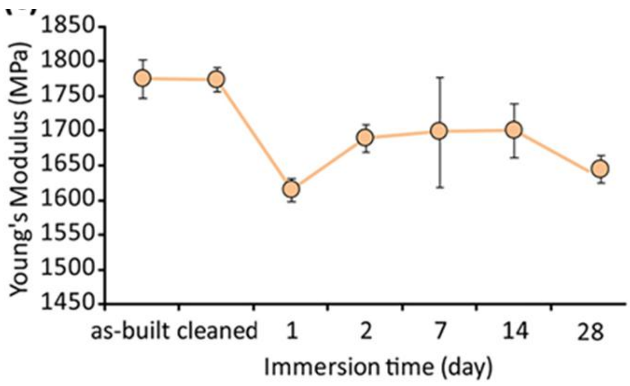

Figure 2.2 - Variation of *E* (MPa) over immersion time for biodegradable Fe (extracted from (Y. Li et al., 2018)).

Recent studies indicate that the current design of AM-Fe scaffolds is more suitable for replacing cancellous bone, which requires lower mechanical strength but high porosity and interconnectivity to promote BR. However, this high porosity reduces mechanical strength. When porosity exceeds 80 percent, there are concerns about σ_y, tensile/compressive strength and fatigue strength, as high initial strength is essential to compensate for the gradual loss of strength during the corrosion process (Bahrudin et al., 2025).

2.2. Mechanical Behaviour of Fe Scaffolds

Fe-based biodegradable structures are considered alternatives to permanent metal implants in non-load-bearing applications, as they can have mechanical properties closer to human bone. Cortical bone, also known as compact bone, forms the outer layer of the structure and has a porosity of only 3 to 5 %. Trabecular bone, on the other hand, is a porous network with a spongy appearance, with a porosity of 50 to 90 %, and is filled with blood vessels and bone marrow (Kontakis et al., 2025).

Scaffolds developed using AM have a porous structure like that of bone. This feature is important for allowing cells to adhere and proliferate. It is therefore essential that the scaffolds have high porosity, permeability and a network of interconnected pores (Lai et al., 2025).

The clinical relevance of porous Fe scaffolds has been demonstrated in vivo. In a one-year study using a porcine ACL reconstruction model, 3D-printed porous Fe interference screws showed progressive degradation, osteointegration, and mechanical stability comparable to Ti implants, confirming their potential for orthopaedic applications (Liu et al., 2025).

Figure 2.3 illustrates the influence of scaffold pore geometry on BR efficiency over a 60-day period. In both subfigures (a) and (b), the horizontal axis (pore_size_x) represents the pore width in the transverse direction of the scaffold, while the vertical axis (pore_size_z) represents the pore height in the longitudinal direction. The colour scale indicates the predicted regeneration performance, where yellow corresponds to higher BR, and red indicates lower efficiency (Perier-Metz et al., 2021).

In subfigure (a), which represents the normalized volume of regenerated bone, the highest values (in yellow) are observed around pore_size_x ≈ 0.7 mm and pore_size_z ≈ 0.8 mm, indicating optimal conditions for bone tissue growth. Subfigure (b) shows a similar trend in regeneration rate, with the best outcomes concentrated in the upper-right region of the graph. When pore_size_x becomes too large, the structural support for cell bridging is reduced, while low pore_size_z values limit vascularization and cellular infiltration. This confirms that a balanced pore geometry—neither too small nor too large—is essential to create a conducive environment for new tissue formation and effective bone healing. Computational models suggest that pore geometries around pore_size_x ≈ 0.7 mm and pore_size_z ≈ 0.8 mm are associated with higher BR volumes, indicating that balanced dimensions may promote favourable mechanical stimuli and tissue growth (Perier-Metz et al., 2021).

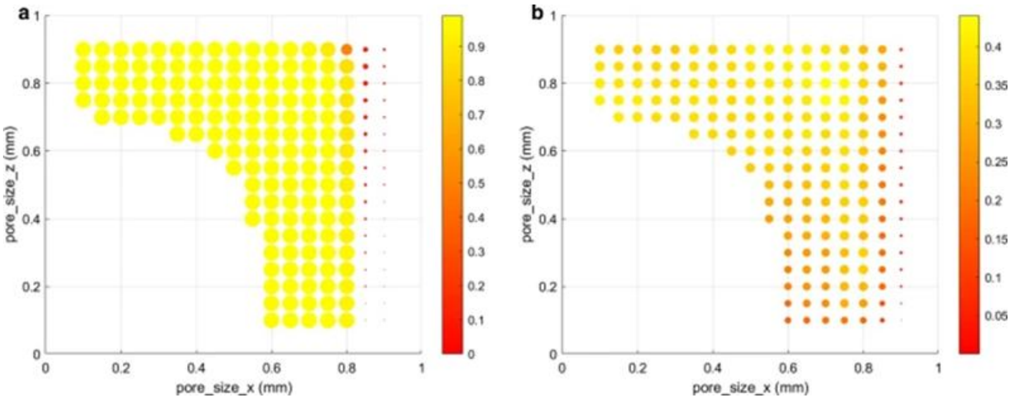

Figure 2.3 - Influence of pore geometry (pore_size_x and pore_size_z) on mechanical stimulation and predicted BR after 60 days (extracted from (Perier-Metz et al., 2021)).

This porous structure and interconnectivity of the pores also help to reduce Fe corrosion, which is normally very slow and not ideal for temporary bone implants. AM processes can produce metal scaffolds with complex and detailed designs, as well as high permeability and interconnectivity of the pores, which promotes tissue growth and controlled corrosion of the Fe scaffolds (Li et al., 2018).

In vivo evidence supports this mechanism. Porous Fe scaffolds implanted in large animal models have shown successful bone integration and gradual degradation over time, validating their role in forming stable interfaces with host bone tissue (Liu et al., 2025).

Fe-based biodegradable structures are considered alternatives to permanent metal implants in non-load-bearing applications, as they can have mechanical properties closer to human bone. The human bone structure consists of two main types of bone: cortical (compact) bone and trabecular (spongy) bone. The outer layer of the structure, cortical bone, has a porosity of only 3 to 5 %. In contrast, trabecular bone is a porous network with a spongy appearance and a porosity of between 50 and 90 % (Lin & Kang, 2021).

This potential has been confirmed in vivo, where porous Fe implants demonstrated sustained mechanical performance and biological integration for over 12 months in a porcine orthopaedic model (Liu et al., 2025).

Fe has strength and hardness properties suitable for BR applications. Compared to other biomaterials used in bone implants, such as Ti and stainless steel, biodegradable Fe contains a combination of mechanical strength and controlled degradability. Fe has a tensile strength and hardness that can be adjusted through manufacturing processes and surface treatments to approximate the properties of bone (Gorejová et al., 2019).

Biodegradable porous Fe produced by AM exhibits mechanical behaviour characterized by an initial elastic phase, followed by continuous plastic deformation without a defined point. This stable response results from the cellular geometry of the structure, which distributes stress evenly and avoids critical concentration. Stress increases progressively until it reaches its maximum value, at which point fracture begins, compromising structural integrity (Rasheed et al., 2023).

2.3. Corrosion in Fe Scaffolds

Corrosion consists of the degradation of Fe due to chemical reactions to the physiological environment. In the human body, the corrosion of Fe is influenced by various factors, including the presence of O_2, Cl^-, the pH of the environment and the composition of body fluids (Gąsior et al., 2021). Although Fe is essential at physiological concentrations (≈10–30 μM), local levels above 50–100 μM can induce the formation of reactive O_2 species via the Fenton reaction, promoting oxidative stress, cell damage, and inflammatory response (Szczęsny et al., 2025). In vitro studies show that Fe^{2+} concentrations above 100 μM significantly reduce the viability of osteoblastic and endothelial cells, with toxicity influenced by the chemical form (soluble or particulate) and the rate of ion release from the implant (Fagali et al., 2020).

Corrosion plays a key role in the efficiency of Fe based biodegradable scaffolds for BTE. The degradation rate of these scaffolds must be carefully controlled to ensure adequate mechanical support while allowing gradual bone integration and growth (Zhou et al., 2023). The bone healing process can take between 6 and 12 months, depending on the severity of the fracture, and Fe degradation must occur at a rate compatible with this period.

The porosity of the scaffold plays a crucial role in regulating the biodegradation of Fe and the formation of bone tissue, as it facilitates the exchange of nutrients and wastes and promotes an environment favourable to cell growth (Putra et al., 2024). Figure 2.4 illustrates the relationship between microporosity and corrosion current, demonstrating that higher porosity initially increases the corrosion rate due to greater electrolyte penetration and surface reactivity. However, at higher porosity levels, the effect plateaus, indicating that other limiting factors such as passivation may become dominant (Sharma & Pandey, 2019).

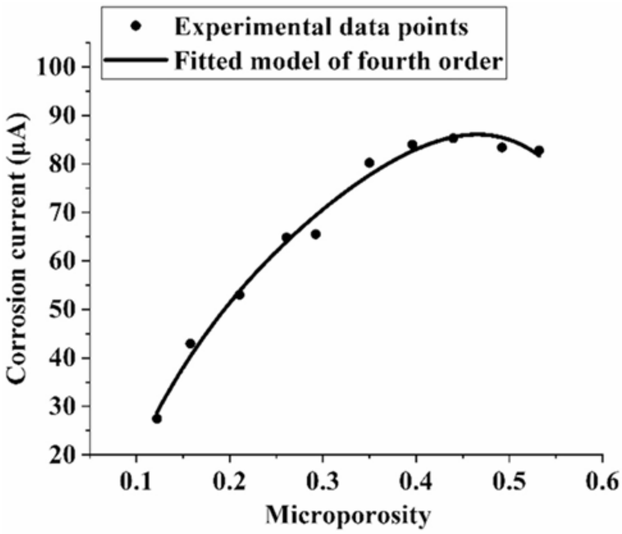

Figure 2.4 - Relationship between microporosity and corrosion current in Fe scaffolds.

Fe-Mn alloys, such as Fe-25% Mn and Fe-35% Mn, exhibit more accelerated corrosion compared to Fe. This behaviour is attributed to the microgalvanic effect caused by the presence of Mn, which intensifies the degradation of Fe. Similarly, Fe-based composites, although less studied, also show higher corrosion rates, possibly due to changes in the electrochemical potential of the phases present. In addition, Fe scaffolds subjected to dynamic immersion corrode more quickly than those in static immersion, since the continuous flow prevents the accumulation of corrosion products on the Fe surface, keeping it constantly exposed to new corrosive reactions (Bahrudin et al., 2025; Zhu et al., 2022).

In a biological context, Fe is an essential trace element for cell growth, O_2 transport and storage, and Ribonucleic Acid (RNA) and Deoxyribonucleic Acid (DNA) synthesis. The daily requirement of Fe in adults varies between 8 and 27 mg. Compared to pure magnesium and pure Zinc, Fe has the lowest standard electrode potential (-0.44 V with respect to the normal hydrogen electrode), indicating a lower corrosion rate of these biodegradable metals. Oxidation of pure Fe in a physiological environment produces Fe^{2+}, while reduction of O_2 produces hydroxide ions which combine to form $Fe(OH)_2$. These compounds can precipitate on the surface of Fe, forming barriers that make it difficult for corrosion to continue. Corrosion products are phagocytized by macrophages, and the systemic distribution of Fe ions can affect various organs. As shown in Figure 2.5, the interaction of Ca, chloride, phosphate and hydroxide ions with the Fe surface leads to the formation of corrosion products (Salama et al., 2022).

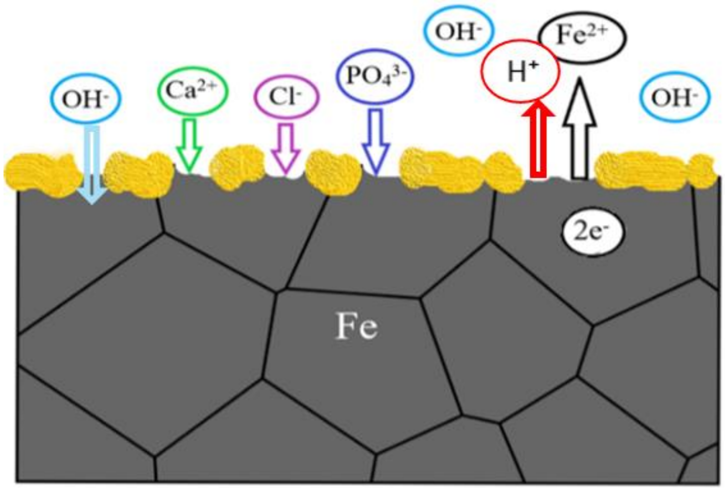

Figure 2.5 - Diagram of metal interface degradation in physiological medium, adapted from (Salama et al., 2022).

The presence of O_2 is essential for catalysing Fe corrosion by participating in cathodic reduction at the metal surface. In the human body, the partial pressure of O_2 under physiological conditions is 30 mmHg, which limits the diffusion of O_2 to the Fe surface. Therefore, the corrosion rate in vivo tends to be lower than in vitro, as laboratory tests are often performed in O_2-saturated solutions (Sakkaf et al., 2022).

For a Fe scaffold to be effective, it must provide mechanical support for the first few months and degrade in a controlled manner to allow replacement by regenerated bone. However, due to its slow degradation, it may be necessary to modify its composition or surface to match its resorption with the optimal bone healing time (Noordin et al., 2025; Percival et al., 2024).

Figure 2.6 illustrates the progression of bone healing and the balance between mechanical stability and material degradation. In the first 7 days, the inflammatory phase involves hematoma formation and immune cell recruitment. Between 3 and 6 months, the functional phase begins with callus formation and increasing mechanical support. From 6 months to 2 years, the resorption phase occurs, where the scaffold degrades and bone remodelling replaces the callus with mature lamellar bone. The lower panel depicts the cellular sequence: hematoma formation, granulation tissue development by mesenchymal cells, differentiation into chondrocytes and osteoblasts, and transition from cancellous to lamellar bone (Sarian et al., 2022).

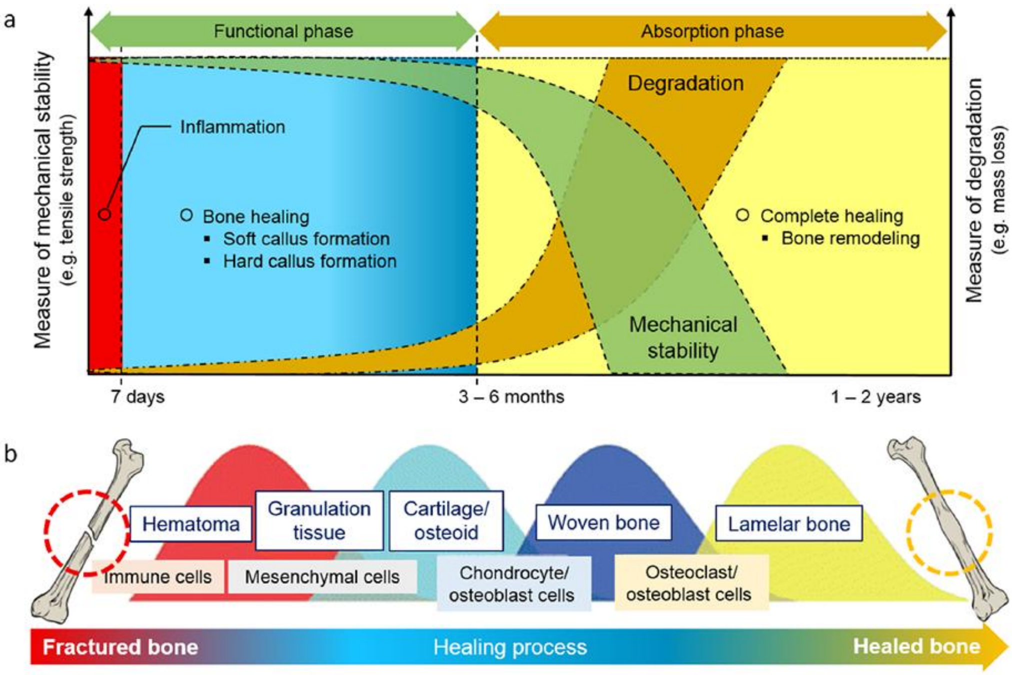

Figure 2.6 - a) Ideal balance between mechanical stability and degradation of absorbable metals during bone healing; b) Sequential phases of fracture healing: inflammation, soft and hard callus formation, and bone remodelling. Colour gradient represents healing progression (extracted from (Sarian et al., 2022)).

OCP measurements are essential for characterizing the electrochemical behaviour of Fe scaffolds in SBF. The OCP reflects the equilibrium potential of the metal in the electrolyte without external current, offering insight into the thermodynamic tendency for corrosion and the stability of the passive layer over time (Noordin et al., 2025).

In physiological environmental, Fe typically shows an initial drop in potential followed by a stabilization phase, which corresponds to the formation of a surface oxide or hydroxide layer ($Fe(OH)_2$, Fe_2O_3 and Fe_3O_4). These compounds can temporarily reduce the corrosion rate by forming a protective barrier, but their stability is highly sensitive to the ionic composition of the medium (Avdeev & Kuznetsov, 2023). Cl^- are known to disrupt films (Wackenrohr et al., 2022). This behaviour has been observed in both static and dynamic immersion conditions, with dynamic flow accelerating film breakdown and exposing fresh metal surfaces to corrosion (Huang et al., 2022; Liu et al., 2025).

Protein adsorption also plays a significant role in modulating OCP. Studies have shown that albumin and fibrinogen can absorbed into Fe surfaces, influencing layer formation and altering degradation kinetics. These interactions contribute to the differences observed between in vitro and in vivo corrosion behaviour (Huang et al., 2022; Wackenrohr et al., 2022).

Additional factors such as temperature (37 °C), blood flow, and protein content further affect the electrochemical response of Fe. The formation and intermittent dissolution of films composed of Fe oxides and hydroxides contribute to OCP variation, with their stability again being compromised by aggressive ions like Cl^- (Cammarata & Mastropasqua, 2023).

Figure 2.7 illustrates the corrosion kinetics of hot-rolled (HR) and electron beam melted (EBM) Fe samples during immersion in modified SBF (m-SBF). Both surfaces were etched in Nital solution for 5 s prior to exposure to standardize surface reactivity. The HR Fe exhibited a rapid drop in OCP, reaching the active corrosion state within minutes, indicating a less stable film and higher initial reactivity. In contrast, the EBM sample showed a prolonged incubation period of approximately 40–50 minutes (m) before transitioning to active corrosion, suggesting a more stable initial surface condition and delayed film breakdown. This difference is likely attributed to microstructural factors, such as grain refinement and reduced defect density in EBM Fe, which enhance layer formation and delay electrochemical activation. These findings reinforce the importance of processing history and surface condition in modulating the degradation behaviour of Fe-based scaffolds in physiological environments (Wackenrohr et al., 2022).

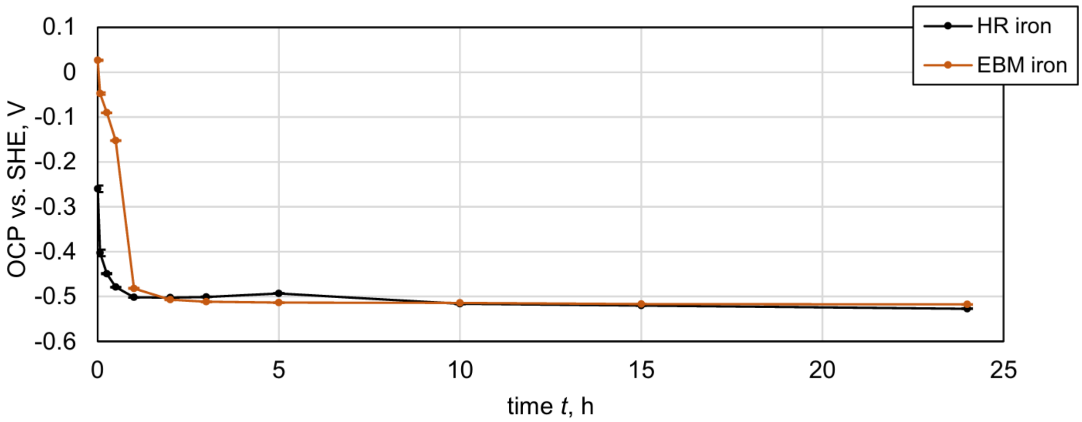

Figure 2.7 - OCP transients of HR and EBM Fe in m-SBF showing faster activation of HR Fe and delayed corrosion onset in EBM Fe due to microstructural differences (extracted from (Wackenrohr et al., 2022)).

EIS is a fundamental technique for evaluating the corrosion behaviour of Fe scaffolds in physiological environments. Figure 2.8 presents Nyquist plots for Fe samples immersed in modified simulated body fluid (m-SBF) at different exposure times (1 h, 6 h, 12 h, and 24 h). The semicircular profiles observed reflect the capacitive behaviour of the electrochemical interface, with the diameter of each semicircle directly related to the charge transfer resistance and, consequently, to the material's corrosion resistance. As shown in Figure 2.8, the sample immersed for 1 h exhibits the largest semicircle, indicating higher corrosion resistance at the initial stage. With increasing immersion time, the semicircles progressively decrease in diameter, especially in the 12 h and 24 h samples, revealing a reduction in charge transfer resistance and an increase in electrochemical activity. This trend is associated with the gradual degradation of films and the accumulation of corrosion products, which alter the metal/electrolyte interface and facilitate ionic transport (Dong et al., 2021).

Additionally, comparative studies show that porosity significantly influences the corrosion resistance of Fe scaffolds. Dense samples display large semicircles in Nyquist plots, indicating high corrosion resistance. In contrast, porous samples exhibit smaller semicircles and a straight line at low frequencies, characteristic of diffusion-controlled processes and lower impedance. This effect is even more pronounced in structures with ordered porosity, which show the lowest impedance values and the highest susceptibility to degradation (Sharma & Pandey, 2019).

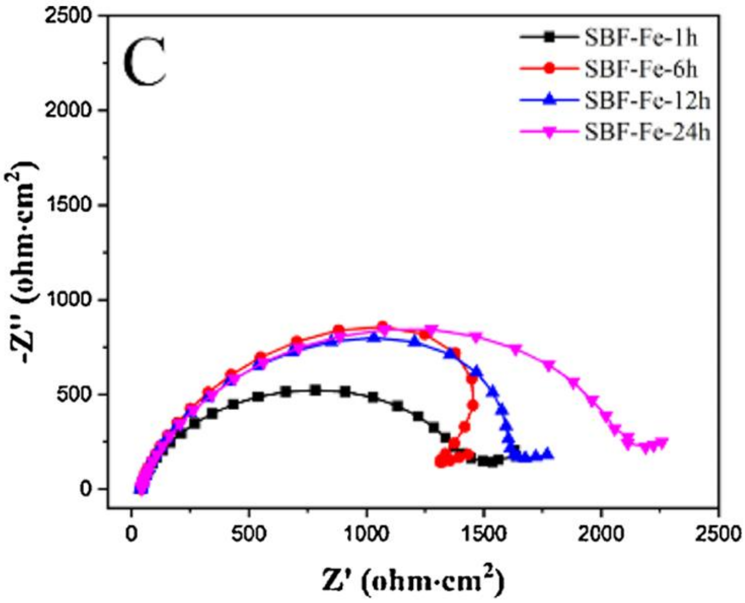

Figure 2.8 - Nyquist plots after 1 h, 6 h,12 h and 24 h immersion (extracted from (Dong et al., 2021)).

Figure 2.9 presents the Bode spectra obtained by EIS for Fe immersed in SBF at different exposure times (1 h, 6 h, 12 h, and 24 h). The analysis of impedance magnitude (|Z|) and phase angle as a function of frequency (f) allows for the evaluation of the evolution of the metal/electrolyte interface over time. After 1 h of immersion, Fe exhibits high impedance values, indicating initial corrosion resistance associated with the formation of a temporary passive layer. As immersion time increases, a progressive decrease in impedance is observed, particularly at medium and low frequencies, suggesting degradation of the protective layer and increased electrochemical activity at the interface.

The phase angle behaviour also changes over time, reflecting shifts in charge transfer mechanisms. The absence of additional time constants in the high-frequency region indicates that no stable protective layers are formed that could generate distinct capacitive responses in this range. These results highlight the dynamic and unstable nature of Fe passivation in physiological environments, with a tendency toward gradual loss of corrosion resistance during immersion (Dong et al., 2021; Herrera Hernández et al., 2020; Liu et al., 2025).

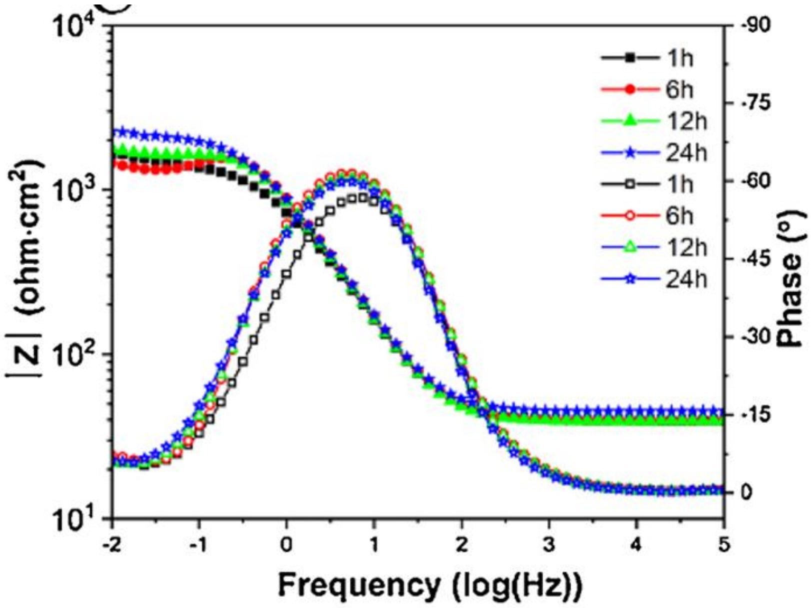

Figure 2.9 - Bode plots after 1 h, 6 h,12 h and 24 h immersion (extracted from (Dong et al., 2021)).

BR applications require a balance between controlled degradation and mechanical strength. Dense Fe, although highly resistant to corrosion, degrades very slowly, which can prevent the implant from being replaced by new bone tissue. Porous scaffolds, on the other hand, corrode more rapidly, facilitating the release of ions essential for bone growth and allowing better integration with the bone. However, excessive corrosion can cause the structure to lose mechanical strength before the bone is fully formed.

Therefore, samples with moderate porosity appear to be the best choice as they allow gradual degradation without compromising the stability of the implant. This demonstrates the importance of adjusting porosity to achieve a balance between biocompatibility, degradation rate and mechanical strength to ensure efficient BR (Sharma & Pandey, 2019).

2.4. Fatigue in Fe Scaffolds

Fatigue in metallic implants is a critical factor affecting the durability and efficacy of biomedical devices, particularly in BR (Patel et al., 2024). Fe implants have been investigated as a promising alternative due to their biodegradability and adequate mechanical properties (L. Zhang et al., 2023). Understanding the fatigue behaviour of these materials is essential to optimise their design and ensure structural longevity.

σ_y and density are two critical parameters for analysing the fatigue behaviour of BR Fe scaffolds (Prakoso et al., 2020). These properties directly influence the mechanical performance of the scaffold and its ability to withstand cyclic loading (fatigue), as well as its integration with the adjacent bone tissue. Analysis of these factors is essential to ensure that the scaffold has sufficient mechanical strength to support the regeneration process without causing negative effects such as stress shielding.

σ_y is the stress at which the material begins to deform plastically. The point at which the material will not return to its original shape when the load is removed. As shown in Figure 2.10, the stress-strain curve of Fe scaffolds after 28 days of immersion in SBF demonstrates that the material retains mechanical integrity, with a clear yield point followed by a strain-hardening region, indicating good mechanical compatibility with bone tissue (Li et al., 2018).

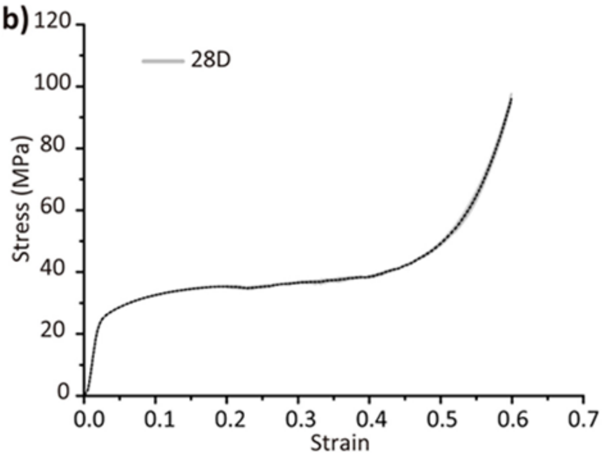

Figure 2.10 - Stress-strain curve of a porous Fe scaffold after 28 days of immersion in SBF, showing the material's deformation behaviour compression test (extracted from (Li et al., 2018)).

In other words, it is the limit between elastic and plastic deformation of a material (Lozhkomoev et al., 2022). The σ_y of Fe is approximately 250 - 500 MPa, depending on the alloy and processing, while cortical bone has values between 100 - 150 MPa and trabecular bone between 2 - 12 MPa (Rezapourian et al., 2022).

Fe has a much higher σ_y than bone, which means it can withstand high loads without permanent deformation. However, this high σ_y can lead to stress shielding - the Fe scaffold absorbs too much load, preventing the adjacent bone from receiving the mechanical stimulus necessary for regeneration. To reduce this effect, Fe scaffolds are often designed with high porosity, which reduces stiffness and brings the mechanical behaviour closer to that of natural bone.

Density reflects mass per unit volume and influences mechanical behaviour and the ability to withstand cyclic loading (fatigue). The density of Fe is approximately 7.87 g/cm³, while cortical bone has a density of approximately 1.85 - 2.0 g/cm³ and trabecular bone between 0.2 - 1.0 g/cm³ (Lozhkomoev et al., 2022).

Fe is approximately 4 to 5 times denser than cortical bone and 8 to 10 times denser than trabecular bone. This difference in density can hinder mechanical adaptation and BR, leading to stress shielding effects and poor bone integration. To mitigate this issue, Fe-based scaffolds are often engineered with controlled porosity (60–80%) porosity, which reduces the effective density and allows for better mechanical compatibility with the bone.

Fatigue analysis is often performed using stress-number of cycles S-N curves, which relate the applied stress to the number of cycles to failure (Putra et al., 2024b; L. Zhang et al., 2023). These curves are essential for predicting the life of the material under cyclic loading conditions. In the case of implants, it is important to consider factors such as stress distribution, the presence of porosity and the effects of the biological environmental on material failure (L. Zhang et al., 2023).

BR with metallic implants requires a balance between mechanical strength and biodegradability (Tonna & Saliba, 2019). An Fe implant must be able to withstand the cyclic loading imposed by the biomechanical environment and allow osseointegration before complete failure. Studies show that the design of porous structures, with control of pore geometry and total porosity, can optimise this behaviour, reduce stress concentration and increase fatigue life.

The fatigue behaviour of metallic implants, particularly those made of Fe, is a critical factor in ensuring their long-term durability and functional performance in BR. This behaviour is commonly assessed using SN curves, which illustrate the relationship between the amplitude of cyclic stress and the number of cycles to failure. These curves are essential for predicting implant lifespan under physiological loading, as they provide insight into the material's resistance to fatigue over time.

Recent experimental results confirm that porous Fe scaffolds subjected to cyclic compressive loading in N_2 exhibit delayed fatigue failure, maintaining structural integrity beyond 3×10^6 cycles at 0.65 σ_y. SEM analysis shows that cracks initiate predominantly at strut junctions, where tensile stresses concentrate, as confirmed by finite element modelling. Despite crack initiation, no complete structural failure was observed, and crack propagation remained localized and slow. Electron Backscatter Diffraction analysis revealed transgranular propagation without preferred orientation, while Kernel Average Misorientation maps indicated higher intragranular misorientation near cracks at higher stress levels (0.90 σ_y). These findings demonstrate that, under compressive fatigue in N_2, Fe scaffolds retain mechanical reliability over extended cycling, supporting their suitability for BR applications where axial loading predominates (Li et al., 2019).

In general, materials with flatter S-N curves exhibit superior fatigue resistance, as they can endure a higher number of cycles at given stress levels before failure. For Fe-based implants, the shape and slope of the S-N curve are influenced by several factors, including microstructure, porosity, surface roughness, and the manufacturing and post-processing techniques employed (Y. Liu et al., n.d.; Putra et al., 2024; Wang et al., 2023). Porous architectures, while beneficial for reducing density and improving osseointegration, may introduce stress concentrators that accelerate crack initiation under cyclic loading (T. Zhang et al., 2025). Likewise, surface defects and residual stresses from AM or machining can significantly affect fatigue life.

The influence of surface finish on implant fatigue is illustrated in Figure 2.11, which shows SEM images taken before and after fatigue testing. This figure enables a comparative analysis between implants that underwent surface treatments, such as sandblasting, and those left untreated after SLM. Untreated implants exhibit irregular surfaces and residual particles from the SLM process, which act as stress concentrators and promote early crack initiation, significantly reducing fatigue life (Anbarzadeh et al., 2023; Zhang et al., 2022). In contrast, sandblasted implants present cleaner and more uniform surfaces, reducing surface defects and delaying crack nucleation.

The presence of cycles exceeding 10^6 in Figure 2.11 highlights the scaffold's performance within the high-cycle fatigue regime. This domain is characterized by predominantly elastic deformation and gradual crack propagation, in contrast to low-cycle fatigue, which typically occurs below 10^4–10^5 cycles and is dominated by plastic strain accumulation. Given that metallic implants are subjected to repetitive biomechanical loads during daily activities, achieving fatigue resistance beyond 10^6 cycles is essential to ensure long-term structural integrity and clinical reliability (Putra et al., 2024; Wang et al., 2023). This region of the S–N curve approaches the fatigue limit the maximum stress amplitude the material can withstand for an effectively infinite number of cycles without failure and is therefore critical for predicting implant longevity under physiological loading conditions.

Figure 2.11 also highlights typical crack initiation sites, often located in rough surface regions with adhered particles. These imperfections generate high local stresses, while internal cracks suggest that inclusions and microstructural heterogeneities also contribute to fatigue failure. The fracture surfaces show two distinct zones: an initiation region with radial striations and a final fracture zone with dimpled morphology, indicative of ductile failure and residual deformation capacity.

Experimental data confirm that surface treatment significantly improves fatigue life in Fe implants. Sandblasted samples withstand more cycles before failure due to reduced roughness and elimination of stress concentrators. This enhancement is reflected in the S–N curves, which show a flatter slope and increased life at lower stress amplitudes (Ordnung et al., 2025). These findings support surface treatment as a viable strategy to optimize implant durability and reduce premature failure risk.

Additionally, Figure 2.11 demonstrates that fatigue failure in Fe implants is progressive and localized, emphasizing the importance of design and manufacturing refinements. Finite Element Analysis can help identify stress concentration zones and guide structural optimization. Moreover, controlling the microstructure through heat treatment or alloying can further enhance fatigue resistance, making Fe implants safer and more effective for clinical use (Sharma & Pandey, 2019).

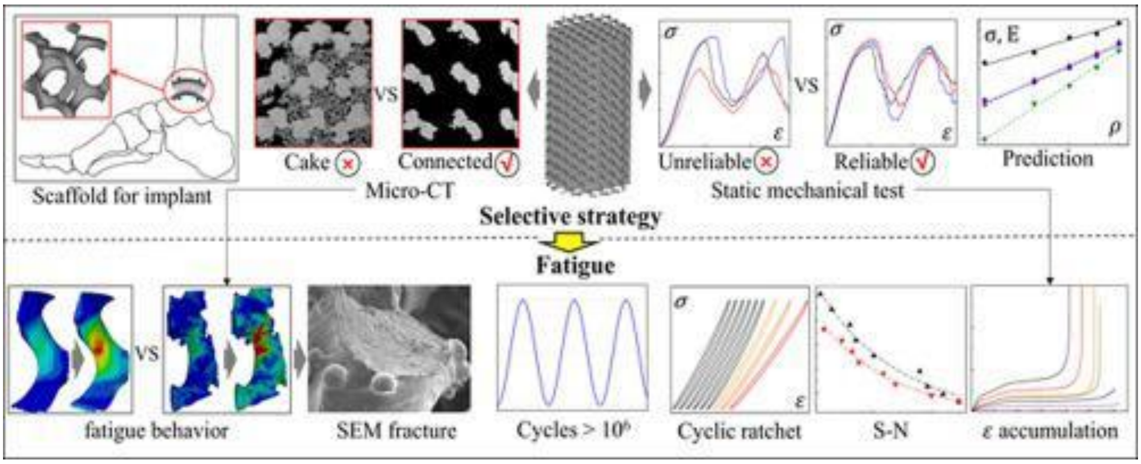

Figure 2.11 - Integrated methodology for evaluating fatigue behaviour of Fe-based scaffolds: from microstructural analysis and mechanical testing to S–N curve prediction and fracture characterization (extracted from (Sharma & Pandey, 2019)).

2.5. Corrosion - Fatigue in Biodegradable Fe Scaffold

Corrosion-fatigue in biodegradable Fe scaffolds manufactured via AM represents a critical challenge to the functional durability of implants in physiological environments. This phenomenon arises from the interaction between cyclic mechanical loading and electrochemical degradation, accelerating structural failure through combined mechanisms (Li et al., 2019). Experimental data show that the biodegradation rate of Fe scaffolds increases significantly under cyclic loading in SBF compared to static immersion, as illustrated in Figure 2.12 b). This acceleration is proportional to the applied stress level, being more pronounced at higher loads such as 0.75 σ_y and 0.90 σ_y. Tests were conducted at a frequency of 15 Hz.

Figure 2.12 e) and f) shows that, under corrosion-fatigue conditions, the concentrations of Ca and phosphorus ions in SBF are significantly lower than those observed under static immersion, indicating greater incorporation of these elements into the corrosion products. For Ca, the differences become significant at stress levels of 0.65 σ_y and 0.75 σ_y, while for phosphorus, the variation is more pronounced at 0.65 σ_y and 0.9 σ_y, reflecting the influence of cyclic loading and the ionic composition of the SBF on the degradation kinetics. The presence of Cl^- promotes localized corrosion, while Ca and phosphate ions may precipitate as protective layers, partially inhibiting corrosion in early stages (Li et al., 2019; Witte et al., 2010). This interpretation is corroborated by EDS analysis, which identifies Fe, Ca, P, O_2, and C in the corrosion products, with significantly higher levels of Ca and potassium in specimens subjected to cyclic loading (Md Yusop et al., 2022). confirming the ionic transfer from the immersion medium to the corroded surface.

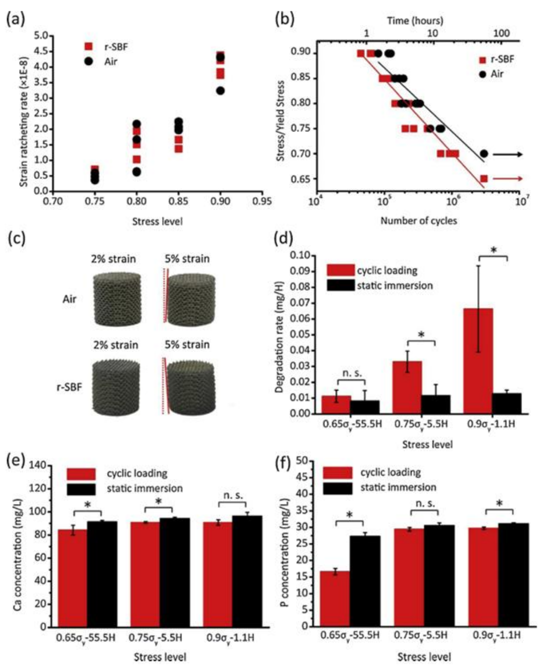

Figure 2.12 - Fatigue behaviour of the AM Fe scaffold specimens in air and in r-SBF: (a) ratcheting rate; (b) S-N curve; (c) failure mode; (d) degradation rate; (e) Ca and (f) P ion concentrations (extracted from (Li et al., 2019)).

SEM analysis revealed that crack initiation predominantly occurs at strut junctions, which are regions of geometric discontinuity and stress concentration. The cracks propagate transgranularly, indicating that failure proceeds through the grains rather than along grain boundaries, and no preferred crystallographic orientation was observed, suggesting that the fracture mechanism is governed by cyclic plastic deformation rather than crystallographic slip systems (Canut et al., 2019; Wang et al., 2023b; Zhao et al., 2022). Similar observations have been reported in Fe–Mn scaffolds fabricated via AM, as illustrated in Figure 2.13. Micro-computed Tomography (Micro-CT) imaging revealed localized cracks initiating at strut junctions and propagating along the scaffold structure, with visible accumulation of corrosion products within micropores. Although the base material differs, the mechanisms of crack nucleation and propagation under corrosion-fatigue, as well as the influence of porous geometry, are comparable and reinforce the interpretation of the results obtained in this study.

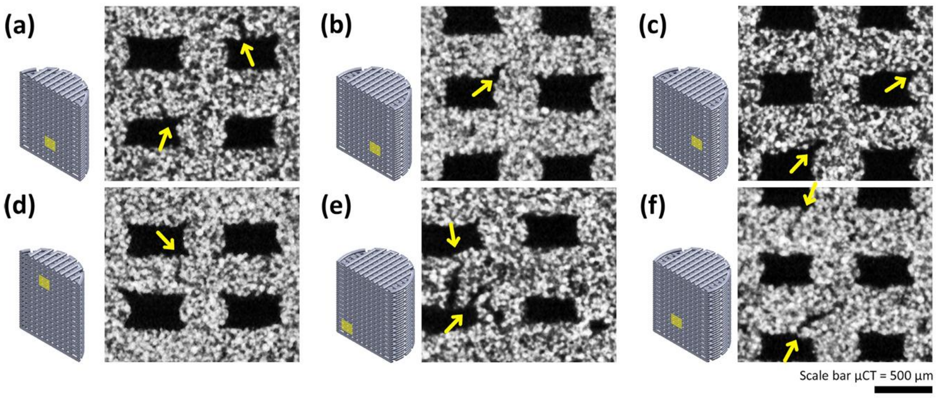

Figure 2.13 - Micro-CT images and 3D reconstructions of Fe–Mn scaffolds after corrosion-fatigue testing (extracted from (Putra et al., 2024)).

The transition from uniform corrosion to localized corrosion-fatigue damage is governed by the accumulation of plastic strain and the breakdown of surface films under cyclic stress. This transition is often marked by the formation of intrusions and extrusions at the microscale, which act as precursors for crack nucleation (Zhao et al., 2022). The Figure 2.14 depicts the sequential stages of degradation under cyclic loading in a physiological environment: (a) electrochemical reactions and progressive breakdown of the protective oxide film due to mechanical stress; (b) formation of locally weakened surface regions; (c) crack initiation at stress concentrators; and (d) subsequent corrosion propagation along the crack path. Although the schematic was originally developed based on observations in Hanks' balanced salt solution, the degradation sequence is comparable to that observed in SBF, as both media induce similar electrochemical–mechanical interactions that drive corrosion-fatigue damage (Md Yusop et al., 2022).

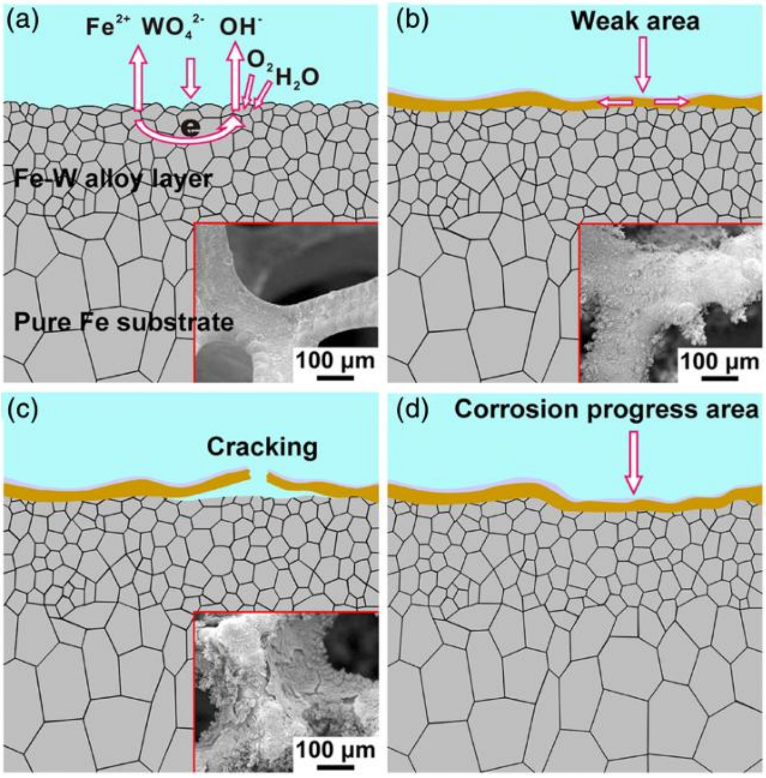

Figure 2.14 - Schematic illustration of the corrosion-fatigue mechanism (extracted from (Md Yusop et al., 2022)).

EIS confirmed that the exposure of new crack surfaces leads to a reduction in polarization resistance and an increase in interfacial capacitance, indicating that these surfaces are highly reactive and accelerate corrosion-fatigue degradation. Even in non-passivating materials, the separation of anodic and cathodic zones after crack formation creates localized microenvironments that promote aggressive propagation (Simões et al., 2022).

These results indicate that corrosion-fatigue is a progressive and localized process that compromises implant integrity over time. It has also been observed that although deformation consistently occurs at the same structural locations under both fatigue and corrosion-fatigue conditions, the presence of a corrosive medium transforms the crack into a continuous source of accelerated degradation. Real-time monitoring of the corrosion potential revealed progressive oscillations with increasing cycle count, evidencing the direct link between mechanical damage and electrochemical instability (Canut et al., 2019).

However, this controlled degradation can be strategically leveraged to synchronize material loss with the progression of BR, ensuring that the scaffold provides mechanical support during the early stages of osteogenesis and is gradually replaced by functional bone tissue.

Chapter 3

Materials and Methods

3.1 Materials

3.1.1. Rod Fe

Before proceeding with the tests on the AM scaffolds, preliminary electrochemical tests were carried out on a solid Fe rod produced using traditional methods to characterize the intrinsic electrochemical behaviour of Fe and establish a baseline reference for comparison.

The preparation of the Fe rod began with the cutting of a segment of suitable size for electrochemical testing. Next, silver conductive glue was used to attach an electrical cable to the end of the rod, ensuring a stable, low-resistance electrical connection with the Potentiostat, which could introduce significant errors in the measurement of potential and impedance.

After the electrical connection was made, the sample was embedded in epoxy resin to isolate the unexposed surfaces and protect the untested areas from corrosion. This procedure allowed the sample to be reused in different tests, ensuring that only the test surface came into contact with the electrolyte solution.

Before the test, the exposed surface was grinded using a BÜHLER Metaserv 2000 polishing machine (serial number 103723) with sandpaper of various sizes (P600, P800, P1000, P2500, and P4000). This process removed corrosion products that may have formed in previous test, resulting in a clean and uniform surface.

3.1.2. 10% Scaffold Fe

The Fe scaffolds used in this study were fabricated using an advanced AM technique, specifically PBF-LB also called Selective Laser Melting (SLM). This method enables the production of complex structures with precise control over geometry, porosity, and microstructure, by selectively melting successive layers of metal powder using a high-energy laser beam guided by a digital CAD model.

The experimental samples were produced using a Renishaw RenAM 500S Flex system, equipped with a 500 W ytterbium fibre laser (λ = 1070 nm) and a spot size of 80 µm, operating in continuous laser modes. The QuantAM 6.0.15.1 software was used to parameterize the print job and generate the build files from the CAD model in. STL format. The PBF-LB process was carried out under an argon atmosphere with 0.0001% residual O_2 content, ensuring minimal oxidation during fabrication.

All scaffolds were fabricated within the RBV of the system, which has a building envelope of 78 × 78 × 50 mm^3, and were printed on a hot-rolled structural steel EN10025 build plate with a thickness of

9 mm and width of 77.4 mm.

The scaffolds were designed using a RTCO unit cell, whose geometry is shown in Figure 3.1, with a) presenting the technical drawing and b) the corresponding isometric view.

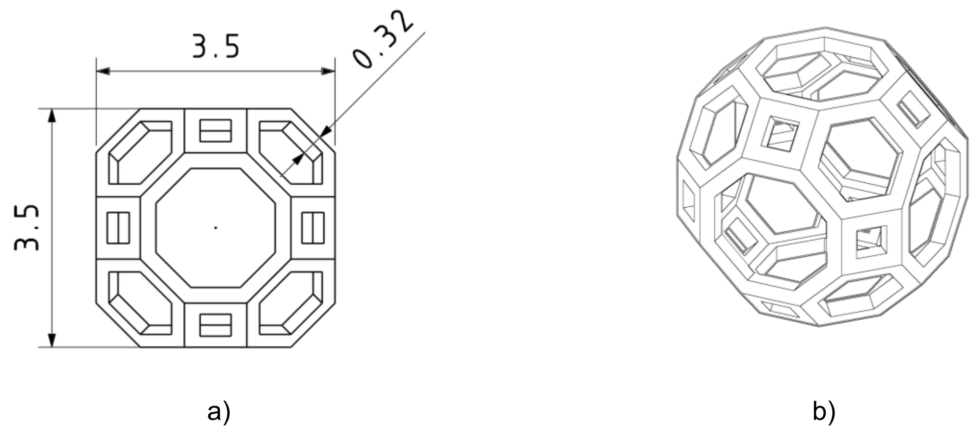

Figure 3.1 - Unit Cell a) technical drawing; b) isometric view.

The scaffold design, illustrated in Figure 3.2, is based on a cylindrical geometry composed of periodically interconnected RTCO unit cells, forming a highly porous network that occupies 10% of the total volume of a fully dense cylinder. This designed porosity aims to reproduce the permeability and mechanical behaviour of cancellous bone, while ensuring adequate space for cell infiltration, nutrient transport, and bone tissue ingrowth throughout the regeneration process.

Figure 3.2 a) shows the technical drawing of the scaffold, detailing the arrangement of the interconnected unit cells and their periodic distribution within the cylindrical geometry. Figure 3.2 b) presents the isometric view, which highlights the overall three-dimensional morphology of the scaffold and the electrical contact, used to connect the specimen to the electrochemical testing system during corrosion and corrosion-fatigue experiments.

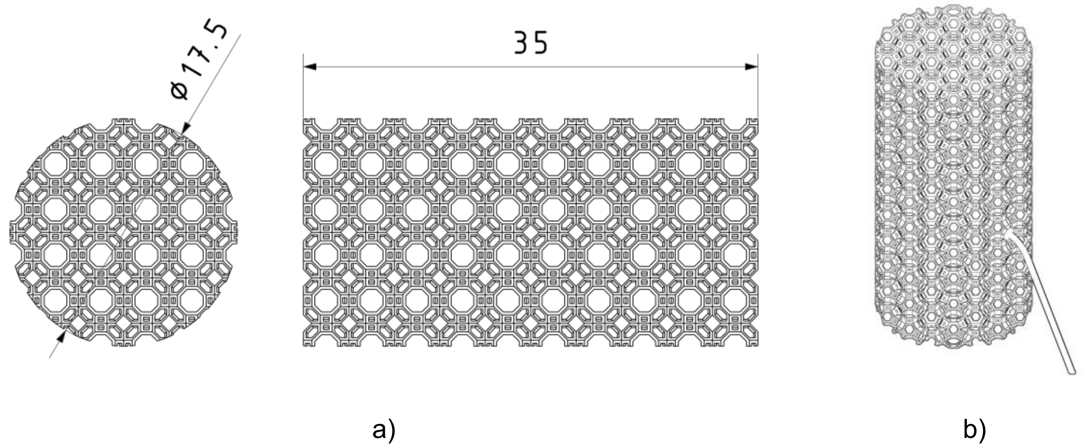

Figure 3.2 – Scaffold a) technical drawing; b) isometric view with electric contact.

For fatigue and corrosion-fatigue testing, the faces of the structure that come into contact with the claws were lightly polished on both sides using a BÜHLER MetaServ 2000 polisher (S/N 103723), with the help of a jig produced by AM, to ensure surfaces became flat and perpendicular to specimen's axis.

After polishing, the samples were measured and cleaned ultrasonically in acetone for 15 + 15 min (two consecutive cycles) in a Transsonic 420 bath (Elma, S/N 103893) to remove unfused powder particles. The structures were then thoroughly dried to prevent any premature corrosion.

The electrical connection was applied only when electrochemical measurements were necessary, in corrosion and corrosion-fatigue test in SBF (for OCP/EIS). In fatigue test in N_2 no electrical connection was used.

For corrosion tests, the same preparation procedure was followed as for fatigue and corrosion-fatigue tests, except that the initial polishing of the contact faces was not required, since the experiment was performed in a three-electrode electrochemical cell where only the exposed surface was in contact with the SBF, without mechanical loading.

3.1.3. Preparation of Simulated Body Fluid (SBF) Solution

The SBF solution was prepared according to the procedure described by Kokubo (Kokubo & Takadama, 2006). All reagents used, listed in Table 3.1, were previously weighed and dissolved sequentially in distilled water and, with dissolution promoted by manual stirring with a glass rod.

After complete dissolution of all reagents, the pH was adjusted to 7.40 ± 0.02 at room temperature using 1 M HCl and monitored with a pH meter (pH 50 VioLab Basic). The final solution remained clear and colourless, with no evidence of precipitation (yellow discoloration), and was subsequently stored in a 1000 mL volumetric flask and kept refrigerated.

Table 3.1 - Preparation of the SBF solution (1000 ml) follow Kokubo formulation (extracted from (Kokubo & Takadama, 2006)).

S. no.	**Reagents**	**Amount in 1000 ml**
1	NaCl	8.035 g
2	$NaHCO_3$	0.355 g
3	KCl	0.225 g
4	$K_2HPO_4 \cdot 3H_2O$	0.231 g
5	$MgCl_2 \cdot 6H_2O$	0.311 g
6	1.0 M HCl	39.0 ml
7	$CaCl_2$	0.292 g
8	Na_2SO_4	0.072 g
9	$((HOCH_2)_3CNH_2)$	6.118 g
10	1.0 M HCl	Appropriate amount for adjusting the pH ≈ 7.4

3.2. Corrosion Tests

3.2.1. Three Electrode Cell

The corrosion test was performed using a three-electrode electrochemical cell with a three-electrode configuration: a reference electrode (RE) is a Saturated Calomel Electrode (SCE), a platinum counter electrode (CE), and the Fe sample as the working electrode (WE) to enable electrochemical measurements of in situ corrosion test in SBF at 37°C and pH=7.4.To maintain experimental stability, the cell was placed inside a Faraday cage to minimize external electromagnetic interference and submerged in a thermostatic water bath to maintain a constant temperature of 37 °C and prevent heat loss. Figure 3.3 a) shows an image of the corrosion test and Figure 3.3 b) shows a diagram of the corrosion test configuration. The electrodes were connected to an Interface 1000 Potentiostat (Gamry Instruments, PA, USA, 11016).

a) b)

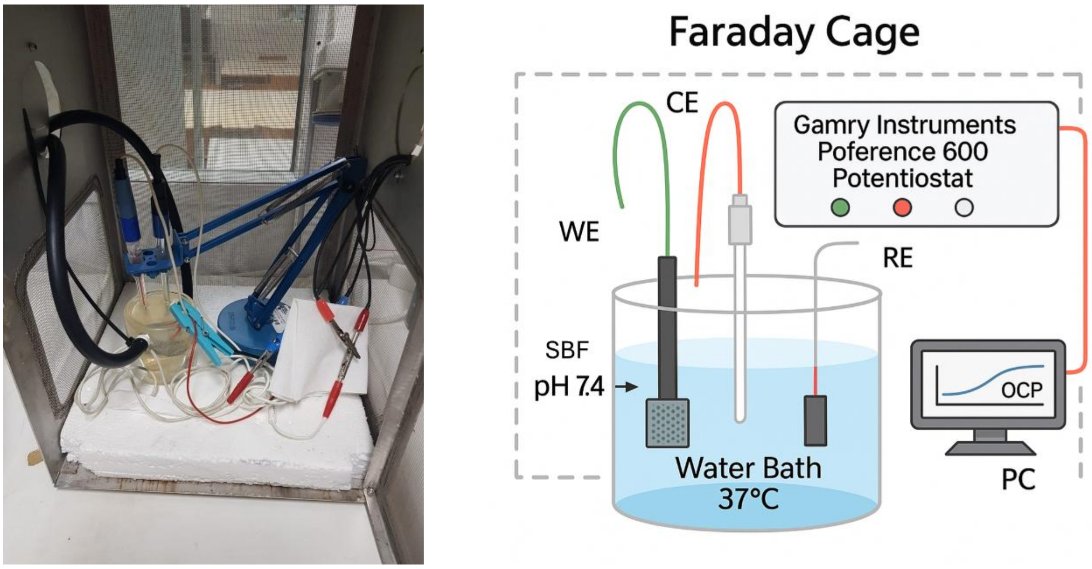

Figure 3.3 - a) Picture and b) schema of the experimental set-up used on corrosion test.

The OCP was monitored over time (mV vs. SCE) to assess how the corrosion potential changed during Fe exposure to SBF. For each test curve, the potential was recorded continuously for 30 minutes. Fe corrosion tests were performed over a total immersion period of 7 days and approximately 1 day for fatigue-corrosion tests. Fe undergoes corrosion processes, and the variation in potential over time allows the identification of corrosive activation phenomena. This made it possible to compare the electrochemical behaviour of the Fe rod and 10% porous scaffolders and to evaluate the differences in terms of stability and corrosion resistance.

EIS tests were performed in SBF, applying a 5 mV sinusoidal signal around the OCP. The frequency range varied between 100 kHz and 3 mHz, providing information on charge transfer resistance, corrosion film formation, and the diffusive processes of ionic species in SBF. The measurements were conducted over 7 days of immersion, allowing the evolution of the electrochemical behaviour of Fe rod and 10% porous scaffolders over time to be evaluated.

3.2 Fatigue Tests in N_2 and in SBF

3.2.1 Testing Machine

Fatigue tests were performed on an inhouse built in-plane test machine, set to uniaxial loading, with horizontal sample mounting on a rigid structure. (Freitas et al., 2014).

Figure 3.4 a) shows the scaffold assembled with N_2, while Figure 3.4 b) illustrates the testing equipment with the fixation region highlighted (red arrows).

The tests were performed in force control mode, applying nominal stress levels between 70% and 90% of the material σ_y = 2.78 MPa. The load ratio was R = 0.1, in compression, the waveform was sinusoidal, and the frequency was 20 Hz in N_2 to maximize performance in an inert environment while maintaining dynamic stability and temperature control. Stop criteria included specimen fracture or compressive deformation more than 10%, loss of load-carrying capacity, or reaching 3×10^6 load cycles (run-out). When no failure occurred by 3×10^6 cycles, the applied nominal stress was recorded as the fatigue strength for that condition. Real-time signals comprised force (calibrated load cell), actuator displacement (internal encoder), and, where applicable, sample deformation via extensometer. Axial alignment was verified using self-aligning devices and controlled clamping torque to minimize eccentricities.

a) b)

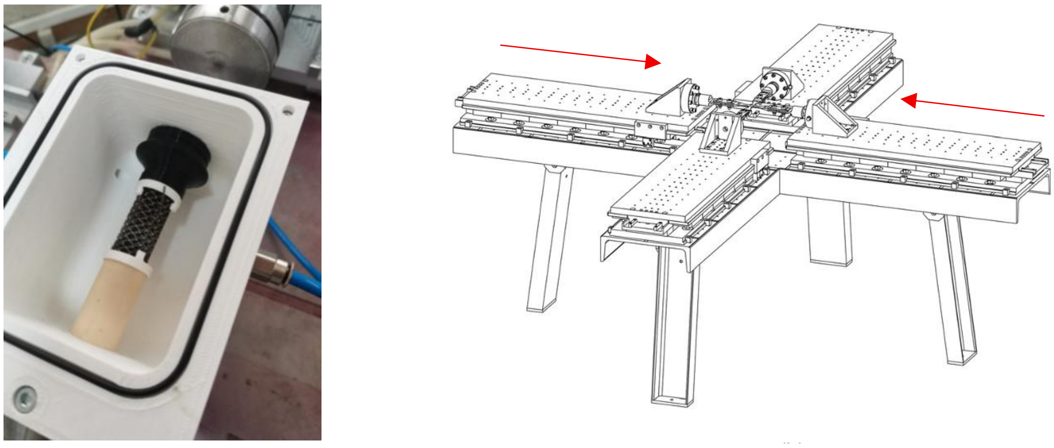

Figure 3.4 - a) Scaffold mounted for fatigue testing in dry N_2; b) Test rig with the fixture/grip region highlighted (red arrows) (extracted from (Freitas et al., 2014)).

Deformation of the scaffolds during testing was monitored using a high-precision optical sensor (Renishaw Vionic, ref. V2BCI30D04BS) (Renishaw, 2025) which can be seen in Figure 3.5. This sensor was mounted to measure the displacement between the two compression plates, which corresponds to the deformation of the sample under testing.

Figure 3.5 - Deformation Sensor – Renishaw Vionic V2BCI30D04BS (extracted from (Renishaw, 2025)).

This incremental encoder offers both high accuracy and a resolution of 20 nm, enabling even the slightest variations in displacement to be detected. This level of sensitivity is essential for strain ratcheting phenomena, the progressive accumulation of deformation over cycles and the transition to instability regimes that precede the structural failure of the scaffold.

The sensor is integrated into the control system of the testing machine, enabling test to be performed in terms of position, force or deformation, or via an external transducer. The equipment specifications ensure high experimental performance, including a maximum static force capacity of ±2.2 kN, a maximum dynamic force capacity of ±3.5 kN, a test frequency of up to 100 Hz (with high stability of up to 20 Hz in complex loads), load cells of ±5 kN, general encoders with a resolution of 1 µm to control da motors, a maximum displacement of 85 mm per motor, and a maximum speed of 1.04 m/s with a theoretical acceleration of 232 m/s².

To determine the σ_y of the scaffold, a monotonic compression test was performed in a dry environment (N_2), applying increasing loads until the sample fractured completely. This test identified the transition point between elastic behaviour and the onset of irreversible plastic deformation, with this value being considered 100% of the σ_y, the specimen has a diameter of 17 mm, a height of 35 mm, and a density of 7.874 g/cm³.The maximum load recorded before structural failure was 1.15 kN, representing the limit capacity of the scaffold under axial compression. The σ_y was determined to be 2.78 MPa, the Young's modulus (E) was 0.56 GPa, and the σ_{max} Maximum normal stress (MPa) reached 4.83 MPa. For comparison, the yield strength of bulk Fe is approximately 432.86 MPa, demonstrating the substantial reduction in mechanical resistance caused by the 90% porosity of the scaffold structure.

Figure 3.6 a) illustrates the scaffold positioned in the electromechanical Impact Testing Machine TS300 SN 380, used for the monotonic compression test. Figure 3.6 b) presents the stress–strain curve obtained until complete fracture of the material. The straight lines represent the 0.2% strain offset used to determine the σ_y according to standard procedures. The compliance of the testing equipment under compression was experimentally determined from which the obtained rigidity of 49.6 N/mm was used to adjust the position values from the test results and thus obtain the corrected stress-strain behaviour of the scaffolds as shown in Figure 3.6 b).

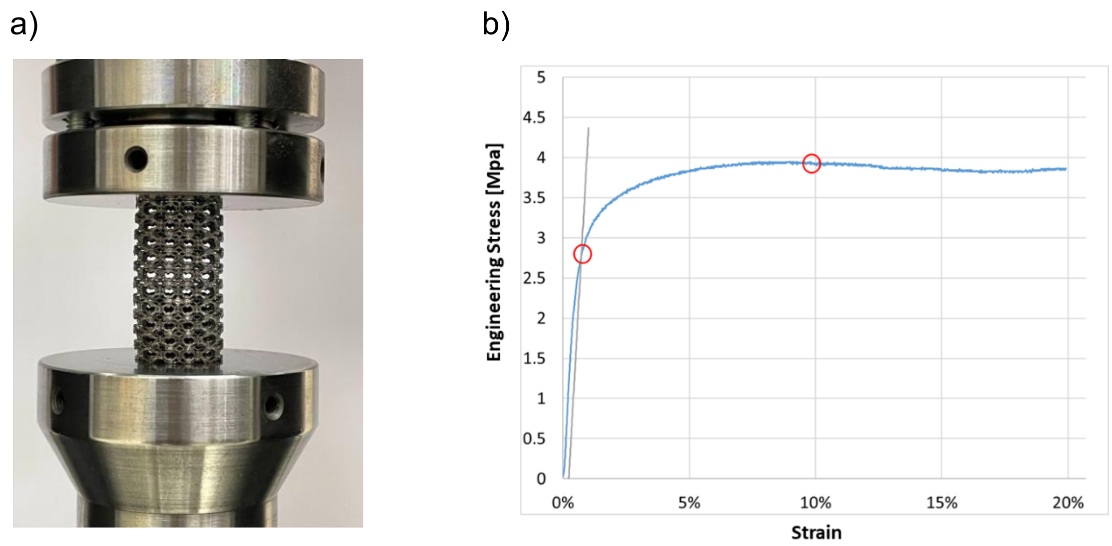

Figure 3.6 - a) Experimental setup for the monotonic compression test. b) Stress–strain curve with 0.002 strain offset used to determine the σ_y.

Based on the σ_y obtained, the mechanical stress levels for the fatigue test were defined, applying percentages of this value to simulate different cyclic loading conditions. This approach made it possible to evaluate the fatigue resistance of the scaffold as a function of the intensity of the applied load, verifying whether progressive extensions occurred throughout the cycles and at what point structural failure began. Higher stresses induce failure in fewer cycles.

The maximum stress applied (σ_{max}) is defined according to the % σ_y chosen in MPa. Equation (3.1) was used to calculate the maximum force (F_{max}) applied to the scaffold, where D is the external diameter of the sample.

$$F_{max} = \frac{\sigma_{max}.\pi.D^2}{4} \quad (3.1)$$

Based on the F_{max} value, it is possible to calculate the minimum force (F_{min}) using the load ratio (R) of 0.1 in compression, which means that the applied σ_{min} is 10% of σ_{max}. To calculate the minimum force applied to the scaffold, Equation (3.2) was used.

$$F_{min} = R.F_{max} \quad (3.2)$$

To reduce noise in the data acquired by the strain sensor and facilitate accurate identification of the scaffold failure point, a VBA (Visual Basic for Applications) code was developed in the form of an Excel macro. This code processes the raw data acquired during the test, applying average filtering.

The logic of the macro consists of grouping the data into blocks of 10 consecutive values, calculating the average of these values, and replacing all 10 original values with the corresponding average value. This procedure eliminates outliers that could distort the analysis, ensuring greater stability and reliability and reducing the large amount of data generated.

To determine the deformation suffered by the structure at each load point, average accumulated deformation(ε_m) was calculated based on the data transmitted by the deformation sensor to the acquisition software and processed by the macro. As the cyclic load is applied, the scaffold gradually reduces height until failure occurs. The sensor records the reduction in height over time, allowing the extension to be quantified in relation to the original dimension, *hs*.

The ε_m was calculated using Equation (3.3):

$$\varepsilon = \frac{\varepsilon_{initial} - \varepsilon_{final}}{hs} \tag{3.3}$$

To analyse the deformation rate over time, the value of mean strain ε_m and alternated strain ε_a during the fatigue cycle and the derivative of the average extension $d\varepsilon_m$ against number of cycles, were calculated as a function of the number of cycles applied. This derivative represents the rate of change in scaffold deformation during cyclic loading, allowing for more accurate identification of the moments when changes occur in the mechanical behaviour of the scaffold, such as the onset of failure or the approach of failure.

In the elastic phase of the test, stress and strain are proportional, and the material returns to its original dimensions as soon as the load is removed. This reversible response is characterized by a linear curve whose slope represents the E. In fatigue, even if the applied stress below elastic limit, close to stress concentrations and potential cracks, there is some local plastic deformation, which accumulates over time, called strain ratchening. In this phase, even after the load is removed, the specimen does not fully recover its original shape, evidencing the presence of residual deformation. The transition between these phases is critical for analysis, as it indicates the onset of cyclic plasticity accumulation, which progressively intensifies until structural failure. The failure criterion chosen was when $\frac{d\varepsilon m}{dN} > \frac{10^{-7}}{cycle}$. This reference value was stabilised by observing curves of several specimens, when it is clearly noticed that a stable regime is being finished and starts a regime where the deformation of the specimen per cycle increases considerably.

Fatigue corrosion test used a similar protocol (R = 0.1 in compression), sinusoidal load and Scaffold). As in this case we have corrosion, that is a time depend variable, the test frequency was reduced to 4 Hz, to replicate human walking/running conditions (Li et al., 2019) The scaffold is in a temperature-controlled environmental cell that exposed the sample to SBF at 37 °C with electrolyte circulation and electrical isolation of the structure with a Faraday cage. Figure 3.7 shows the test in operation, and also shows the Fe scaffolding immersed in SBF inside the cage. The yellowish electrolyte is visible, which is the result of corrosion products after the test. When performed, electrochemical monitoring OCP was run in parallel using a Gamry Reference 600, with acquisition windows synchronized with the mechanical load to avoid measurement artifacts. Average of all signals were continuously acquired at 1 Hz and at a user defined number of cycles at 1000 Hz, during 5 s. This includes the deformation on the sample and the OCP. The instrumentation and alignment procedures corresponded to those of the fatigue test.

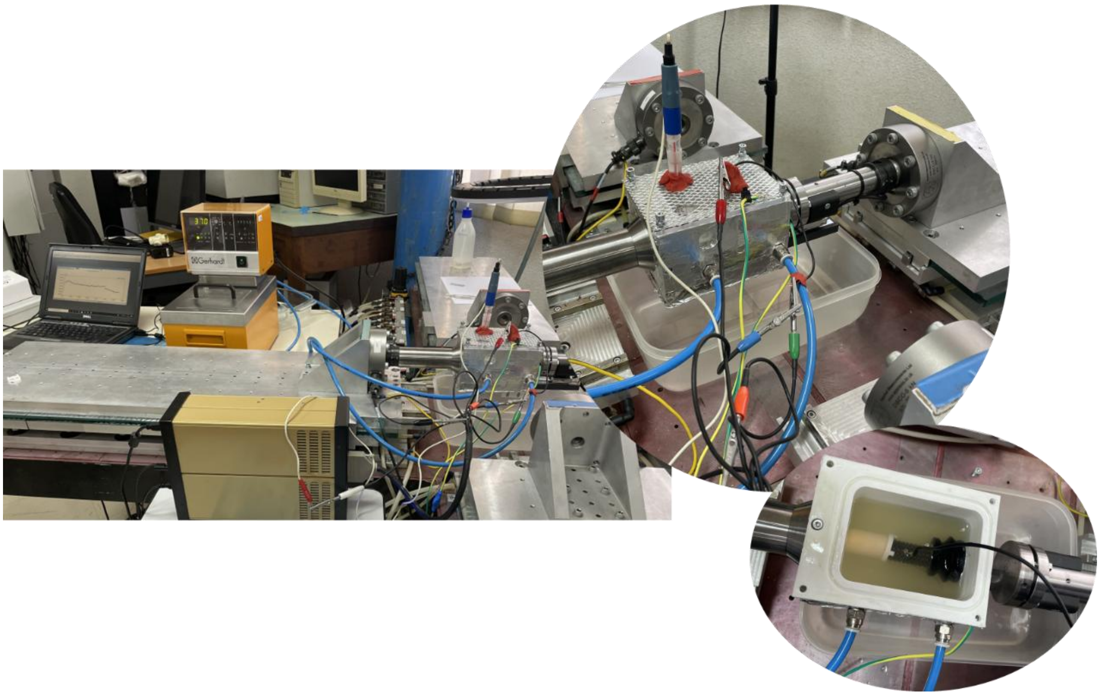

Figure 3.7 – Whole setup of the testing machine and Fe structure after corrosion-fatigue testing immersed in SBF (37 °C) inside a Faraday cage; yellowish electrolyte from post-test corrosion products.

In this test, SBF was used as the medium, with the aim of simulating physiological conditions relevant to biomedical applications. As described in fatigue test in N_2, the same mechanical characterization methods were applied, including the calculation of ε_m, $d\varepsilon_m$, and the failure criterion based on a strain accumulation rate equal to 10^{-7}.

Deformation on the sample was continuously monitored using the Renishaw Vionic V2BCI30D04BS sensor, and the instantaneous corrosion potential was also measured, allowing real-time monitoring of the electrochemical activity of the scaffold surface. Maintaining these procedures allows for a direct comparison between the results obtained in a dry environment and in SBF, enabling accurate assessment of the impact of the corrosive environment on the fatigue behaviour of the material.

As described in the fatigue in N_2, a VBA code in the form of an Excel macro was used to apply average filtering to the data acquired by the strain sensor. This same procedure was maintained for the treatment of potential data, with the aim of reducing experimental noise and ensuring greater stability in identifying the failure point of the scaffold. The grouping and replacement by averages logic, previously detailed, proved effective in both mechanical and electrochemical analysis, ensuring consistency in the interpretation of results.

The measurement of corrosion potential was performed using the same method described previously in fatigue N_2.

The average corrosion potential (E_m) [mV vs SCE] corresponds to the electrochemical value of the scaffold surface in relation to SCE, from the signal acquired at 1 kHz, averaged for a complete loading cycle, reflecting its tendency to oxidize in the physiological environment. Continuous measurement of E_m allowed real-time monitoring of the evolution of electrochemical activity during cyclic loading.

The alternating potential (E_a) [mV] represents the amplitude of fluctuation of the corrosion potential during cyclic loading, from the signal acquired at 1 kHz. It quantifies the electrochemical response of the scaffold surface to the applied mechanical stress, indicating the degree of instability of the film. Larger E_a values correspond to stronger potential oscillations, suggesting increased disruption and surface layer as cracks initiate and propagate.

3.3. Scaffolds Characterization

3.3.1. Fourier Transform Infrared spectroscopy (ATR – FTIR)

The chemical composition and functional groups present on the surface of the corrosion products were analyzed using FTIR. The spectra were obtained with a Nicolet 5700 FT-IR spectrometer (Thermo Electron Corporation, USA), operating in the range of 3500–500 cm^{-1}, using attenuated total reflectance (ATR) mode with a diamond crystal. FTIR allowed the identification of characteristic bands associated with Fe oxides, Fe hydroxide, and phosphate species, providing complementary evidence of the chemical nature of the corrosion products formed during immersion in SBF.

3.3.2. X-ray tomography/Micro – CT

The internal architecture of the Fe scaffolds was analysed using Micro-CT. Scans were performed under dry conditions using the TomoScope X5 Plus system, enabling the acquisition of non-destructive three-dimensional images of the internal structure of the scaffolds.

The acquired data were reconstructed using MyVGL Viewer software, allowing visualization of the structural integrity and fracture zones of the struts resulting from fatigue tests in N_2 and in SBF.

3.3.3. Illuminated Stereo Microscope

The surface observation of corrosion products exposed on Fe rods in corrosion test was performed using a Leica Zoom 2000, Model No. Z30V 240Vac stereomicroscope at 20 - 50× magnification. This technique enabled direct visual inspection of affected areas, facilitating the preliminary identification of surface deposits, morphological changes, and distribution of corrosion products.

3.3.4. Scanning Electron Microscopy (SEM) and Energy Dispersive X-ray Spectroscopy (EDS)

The surface morphology and microstructural features of the samples were examined using SEM. This technique enabled high-resolution visualization of the distribution of corrosion products, pore architecture, and localized degradation zones, providing morphological evidence that complemented the electrochemical data. Additionally, SEM was also employed to analyse the fracture surfaces of the scaffolds after fatigue and corrosion-fatigue tests, allowing detailed observation of crack initiation sites, propagation paths, and failure mechanisms.

The elemental composition of the corrosion products was assessed using EDS, coupled with SEM. EDS allows qualitative and semi-quantitative identification of chemical elements by detecting characteristic X-rays emitted from the sample upon excitation by an electron beam. Spectra were acquired in selected regions to map the distribution of key elements such as Fe oxides, hydroxides, and phosphate-based compounds formed during immersion in SBF.

All analyses were performed using a Hitachi S2400 SEM (Tokyo, Japan), which provided topographical imaging with an enhanced depth of field (50–800 μm at 30-500× magnification).

Chapter 4

Results

4.1. Corrosion behaviour

Figure 4.1 shows the evolution of the OCP for the Fe rod a) and the Fe scaffold b) during immersion in SBF. At the beginning of the test (0 h), both samples exhibited more negative potential values, indicating a highly active metal surface. After 6 h of immersion, the potential of both samples changed to more noble values.

For longer immersion times (1, 3, and 7 days), the potential progressively returned to more negative values in both cases.

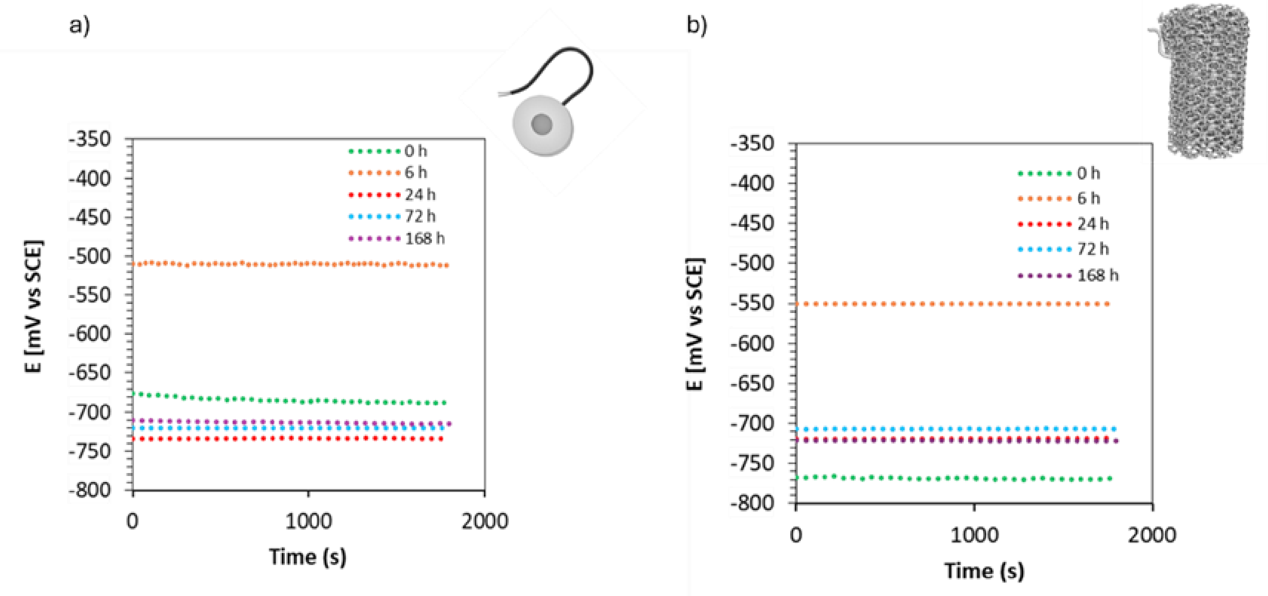

Figure 4.1 - Potential measured in SBF for (a) Fe rod and (b) Fe scaffold, over 7 days of immersion.

Figure 4.2 shows the evolution of the potential over approximately 20 h in SBF for the Fe rod and Fe scaffold under corrosion conditions a) and for the Fe scaffold under corrosion-fatigue conditions b). In both cases, an initial increase in potential is observed during the first hours, associated with the formation of film that enhances surface nobility and temporarily reduces the corrosion rate. However, it is clear that the scaffold in both a) and b) does not reach potentials as noble as those of the Fe rod, stabilizing around –650 mV. It is noteworthy that, in Figure 4.1 b), the scaffold exposed only to the corrosive medium (without cyclic loading) reached values close to –550 mV, indicating a more noble behaviour in the absence of mechanical solicitation. After approximately 12 h, both in a) and b), a sharp decrease in potential to around –750 mV is observed, indicating partial breakdown of the protective layer and subsequent re-exposure of the metallic substrate to the corrosive environment.

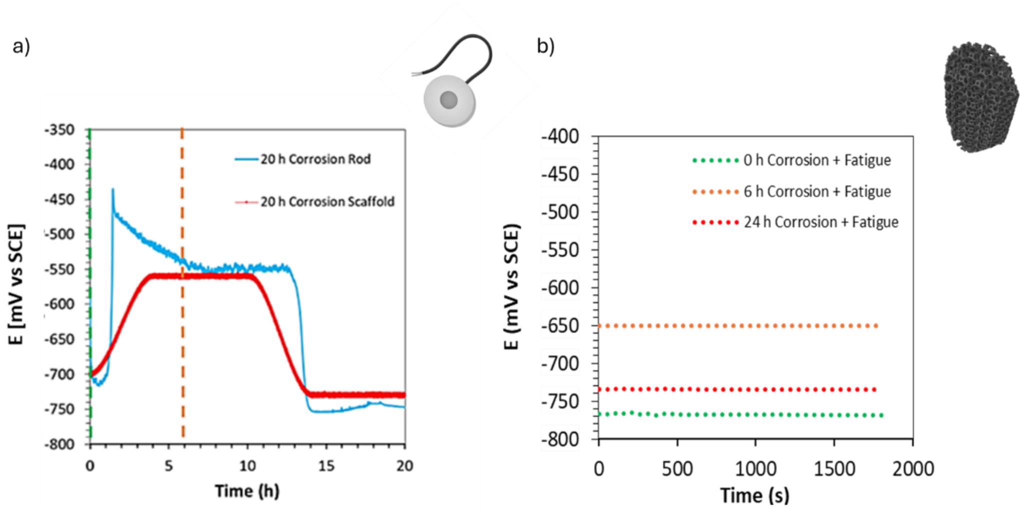

Figure 4.2 - Evolution of OCP in SBF solution over 20 h for the for the Fe rod and Fe scaffold under corrosion conditions a) and for the Fe scaffold under corrosion-fatigue conditions b).

Figure 4.3 presents the comparison between the potential of the Fe scaffold under corrosion and corrosion-fatigue conditions over a period of approximately 24 h. It is observed that, after about 6 h, in the corrosion test the potential becomes more noble, reaching values close to –450 mV, while under corrosion-fatigue conditions the potential remains less noble, around –650 mV. The potential difference observed after 6 h indicates that the application of cyclic stresses compromises the stability and protective capacity of the film. The corrosion test exhibits greater potential instability, characterized by fluctuations associated with local ruptures in the film, which re-expose the metallic substrate to the electrolyte and reactivate the corrosion process.

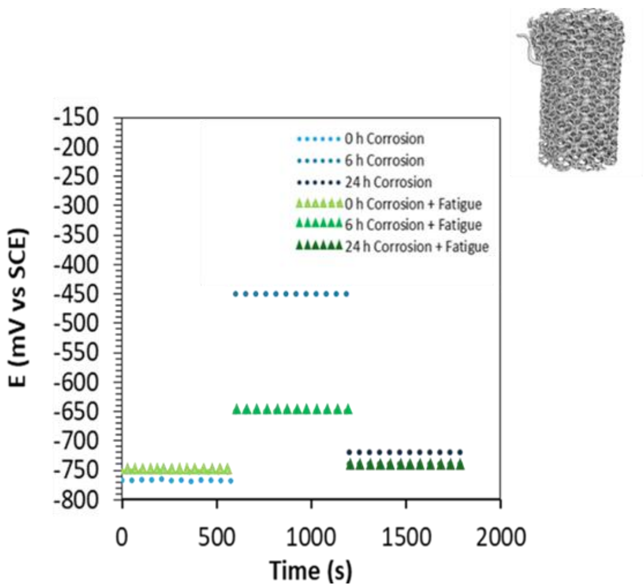

Figure 4.3 - Comparison of the evolution of OCP for the Fe scaffold in corrosion testing and corrosion-fatigue testing for approximately 24 h in SBF solution.

Impedance measurements presented by Nyquist diagram (Figure 4.4) obtained for the Fe rod immersed in the SBF solution at different exposure times (0, 6, and 24 h), represent the frequency response of the electrochemical system, relating the real (Z') and imaginary (Z") parts of the impedance. At 0 h, a semicircle with a reduced diameter is observed, indicating low impedance and a highly active metal surface in direct contact with the electrolyte. After 6 h of immersion, the diameter of the semicircle increases, revealing a flattening of the semicircle. After 24 h, the diagram still shows a large semicircle diameter, but a slight flattening of the curve and a positive curvature of Z'' at low frequencies can be observed. Macroscopic and microscopic observations after 24 h of immersion reveal localized areas of corrosion, where discontinuities in the surface film are visible with partially exposing of the metal surface.

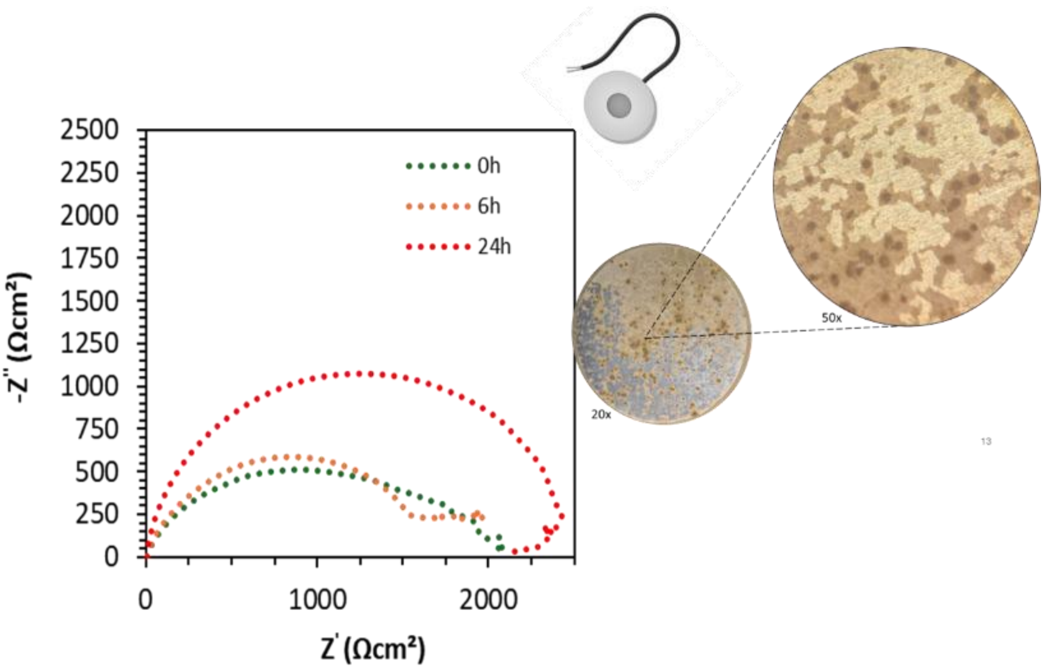

Figure 4.4 - Nyquist diagram for Fe rod in SBF at different exposure times. Optical images, after 24 h immersion.

The Bode diagrams (Figure 4.5), obtained for the Fe rod a) and the Fe scaffold b) after different exposure times in SBF, show the evolution of the impedance modulus (|Z|) and the phase angle (θ) as a function of frequency (log f).

For the Fe rod (Figure 4.5 a), after 6 h of immersion a pronounced increase in |Z| is observed, rising from approximately 10^2 to 10^3 Ωcm^2, accompanied by a leftward shift of the phase peak to lower frequencies.

In the case of the Fe scaffold (Figure 4.5 b), the initial hours reveal a moderate increase in |Z| and a decrease in θ, with impedance values increasing from 10^5 to 10^6 Ωcm^2, associated with more negative phase angles.

In both systems, the leftward shift of the phase angle indicates enhanced surface reactivity with the medium, reflecting progressive changes in the electrochemical properties over the immersion period.

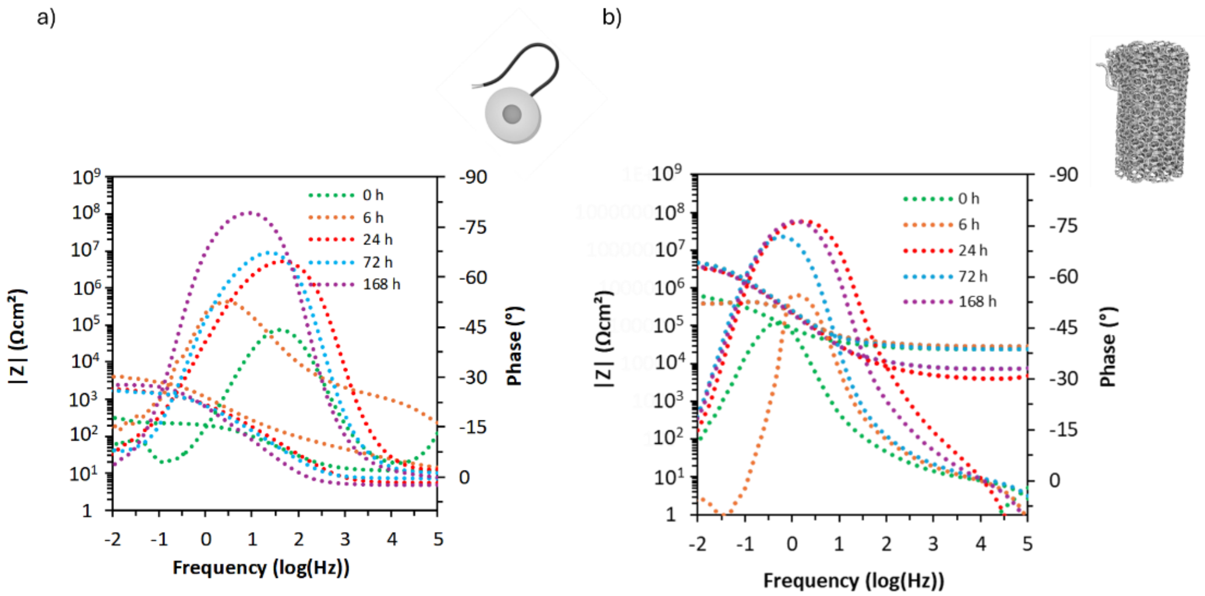

Figure 4.5 - Bode diagrams of the rod (a) and scaffold (b) of Fe immersed in SBF.

Figure 4.6 a) presents the FTIR-ATR spectra corrosion products of the corrosion-fatigue test on the scaffold after 24h. Characteristic bands corresponding to hydroxyl (O–H), carbonate (CO_3^{2-}), and phosphate (PO_4^{3-}) groups are observed, which are typical of corrosion products formed in physiological environments. The broad bands between 3600–3000 cm^{-1} and 1628 cm^{-1} are attributed to the stretching and bending vibrations of the O–H group, respectively, associated with the presence of hydroxides and adsorbed water. The peak near 2875 cm^{-1} corresponds to the stretching vibrations of C–H bonds. The absorption bands between 1368 cm^{-1} and 1050 cm^{-1} are related to carbonate and phosphate groups. In particular, the asymmetric stretching v_3 (C–O) of CO_3^{2-} is identified at 1368 cm^{-1}, the asymmetric v_1 (C–O) vibration is observed near 1050 cm^{-1}, and the asymmetric v_2 (CO_3^{2-}) mode occurs around 877 cm^{-1}.

Complementarily, Figure 4.6 b) shows the monitoring of the pH variation of the SBF solution during the scaffold corrosion test over 168 h of immersion. A slight decrease in pH is observed over time, associated with the formation and accumulation of corrosion products. This trend reflects the partial consumption of OH^- ions and the release of H^+ ions resulting from the electrochemical oxidation reactions of iron, contributing to a gradual decrease in pH.

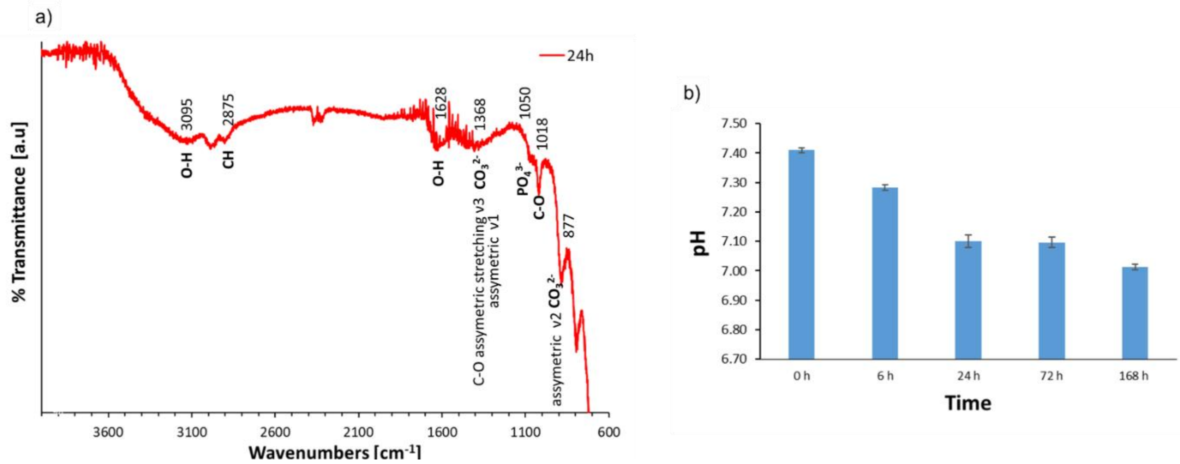

Figure 4.6 – FTIR-ATR spectra corrosion products of the corrosion-fatigue test on the scaffold after 24h a); pH evolution of SBF during scaffold immersion over time b).

4.2. Fatigue behaviour

Fatigue tests were performed in order to evaluate the fatigue behaviour of Fe structures, under inert medium (N_2).

To better establish a criterium for the end of the fatigue test, the signal of the deformation on the sample, was analysed in terms of mean strain, ε_m (Figure 4.7 a) and b)), $d\varepsilon_m/dN$ (Figure 4.7 c) and d)) and stain amplitude ε_a (Figure 4.7 e) and f)), during a fatigue cycle against number of cycles. As the derivative is more sensitive to variations, small deviations or changes in the trend of ε_m manifest themselves as peaks (damage increase) or valleys (stabilization). To avoid false peaks induced by network noise, the signal was previously smoothed, and the derivative used was the average of 10 of the 10 cycles, with outliers removed from the average, thus smoothing the signal. Through this differential analysis, the point at which the transition from stable to unstable deformation occurs becomes more evident, which is associated with the beginning of the structure's failure process. This behaviour is identified by the sharp increase in the $d\varepsilon_m/dN$ – N curves, indicating a sudden acceleration in the accumulated deformation. This point of sudden acceleration is evident for all samples at $d\varepsilon_m/dN$=1E-7 /cycle, as it can be confirmed by the vertical red line that is represented in all graphs of Figure 4.7.

Figure 4.7 c) shows the $d\varepsilon_m/dN$ - N curves obtained under different load conditions: at 70% of the maximum load, the accumulation rate remained low and stable for most of the fatigue life, with a sudden increase at cycles 2501000, and at 90% Figure 4.7 d), this transition occurred earlier and with a higher strain rate at 236000 cycles. Figure 4.7 e) and f) illustrate the ε_a - N evolution, confirming the stable cyclic behaviour during most of the fatigue life, followed by a rapid strain accumulation immediately before failure.

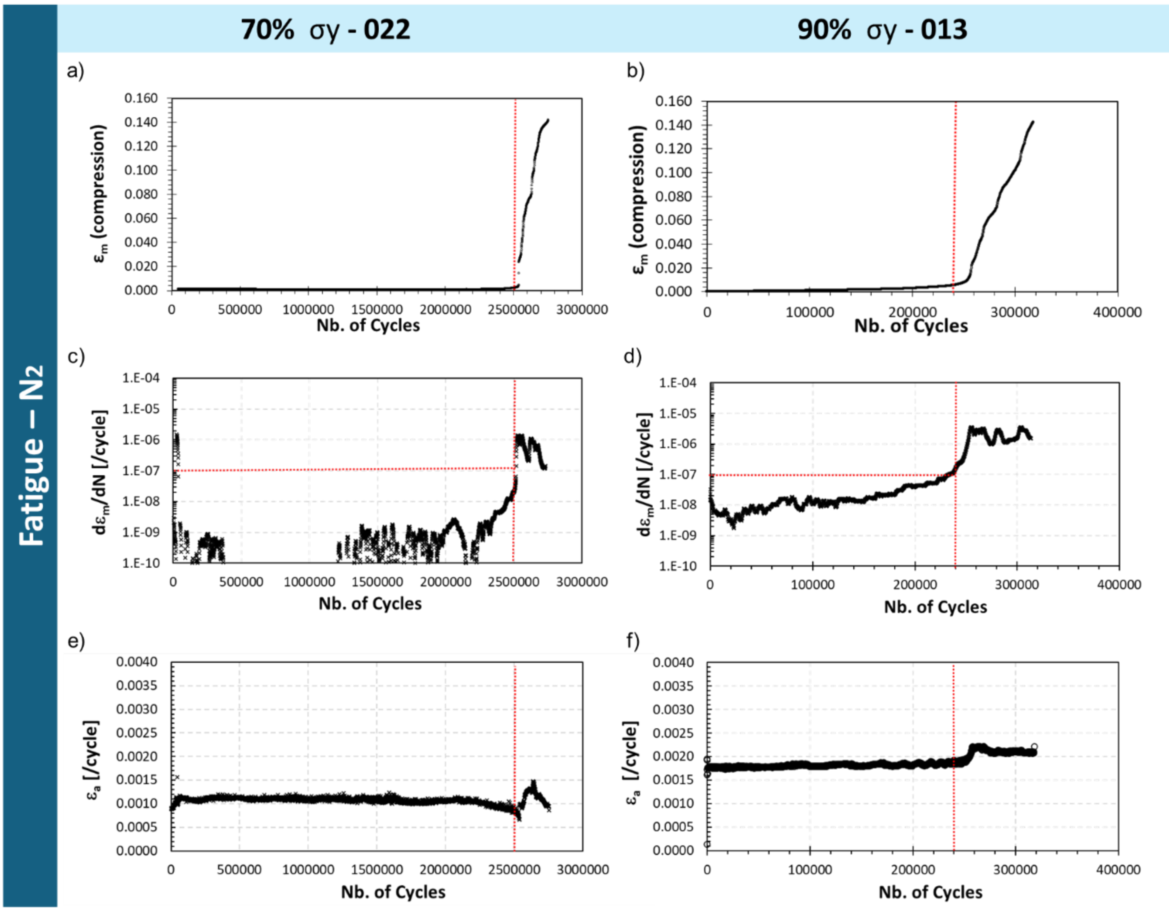

Figure 4.7 - Curves of Fe scaffolds under different conditions, in N_2: a) ε_m–N curve fatigue at 70% σ_y, b) ε_m–N curve fatigue at 90% σ_y, c) $d\varepsilon_m/dN$ vs N curve fatigue at 70% σ_y and d) $d\varepsilon_m/dN$ vs N curve fatigue at 90% σ_y e) ε_a–N curve fatigue at 70% σ_y, e f) b) ε_a–N curve fatigue at 90%.

In SBF, samples loaded at 60% of the σ_y had a substantially longer service life than those loaded at 90%, confirming the reduction in durability with increasing stress, as can be seen in Figure 4.8 a) and b), and in agreement with the fatigue results in inert N_2 medium, Figure 4.7 a) and b).

Analysing the results, at 60% of the maximum load, the accumulation rate remained low and stable for most of fatigue life, with an increase at 228993 Figure 4.8 d), the transition occurred earlier, at 151000 cycles. Figure 4.8 e) and f) illustrate the ε_a - N evolution, confirming the stable cyclic behaviour during most of the fatigue life, followed by a rapid strain accumulation immediately before failure.

In Figure 4.8 g) and h), the relationship between the differential strain accumulation rate ($d\varepsilon_m/dN$) and the average OCP (E_m) is shown. Samples tested at 60% of σ_y exhibited a considerably longer fatigue life compared to those at 90% of σ_y, confirming that higher stress accelerates both plastic strain accumulation and potential fluctuations, indicating increased electrochemical instability at the surface. Figure 4.8 i) and j) show the correlation between the strain amplitude normalized by stress (ε_a/σ_a) and the alternating potential (E_a). At 60% of σ_y, the amplitude remained stable throughout the test, while at 90% of σ_y, a sharp rise occurred near failure, suggesting accelerated degradation and loss of structural integrity, consistent with intensified electrochemical oscillations.

As previously done in the fatigue results, to better characterize the deformation process throughout the fatigue test, the mean strain, ε_m, $d\varepsilon_m/dN$ and stain amplitude ε_a, during a fatigue cycle were analysed against number of cycles. Also the average (E_m) and the amplitude (E_a) of OCP were analysed against the number of cycles to evaluate if any of these measurements are enough sensitive to fatigue damage, to be used as a criterium for fatigue life determination.

Once again, $d\varepsilon_m/dN$=1E-7 /cycle, as shown to provide a good criterium for fatigue life, as it can be confirmed by the vertical red line that is represented in all graphs of Figure 4.8, under different load conditions.

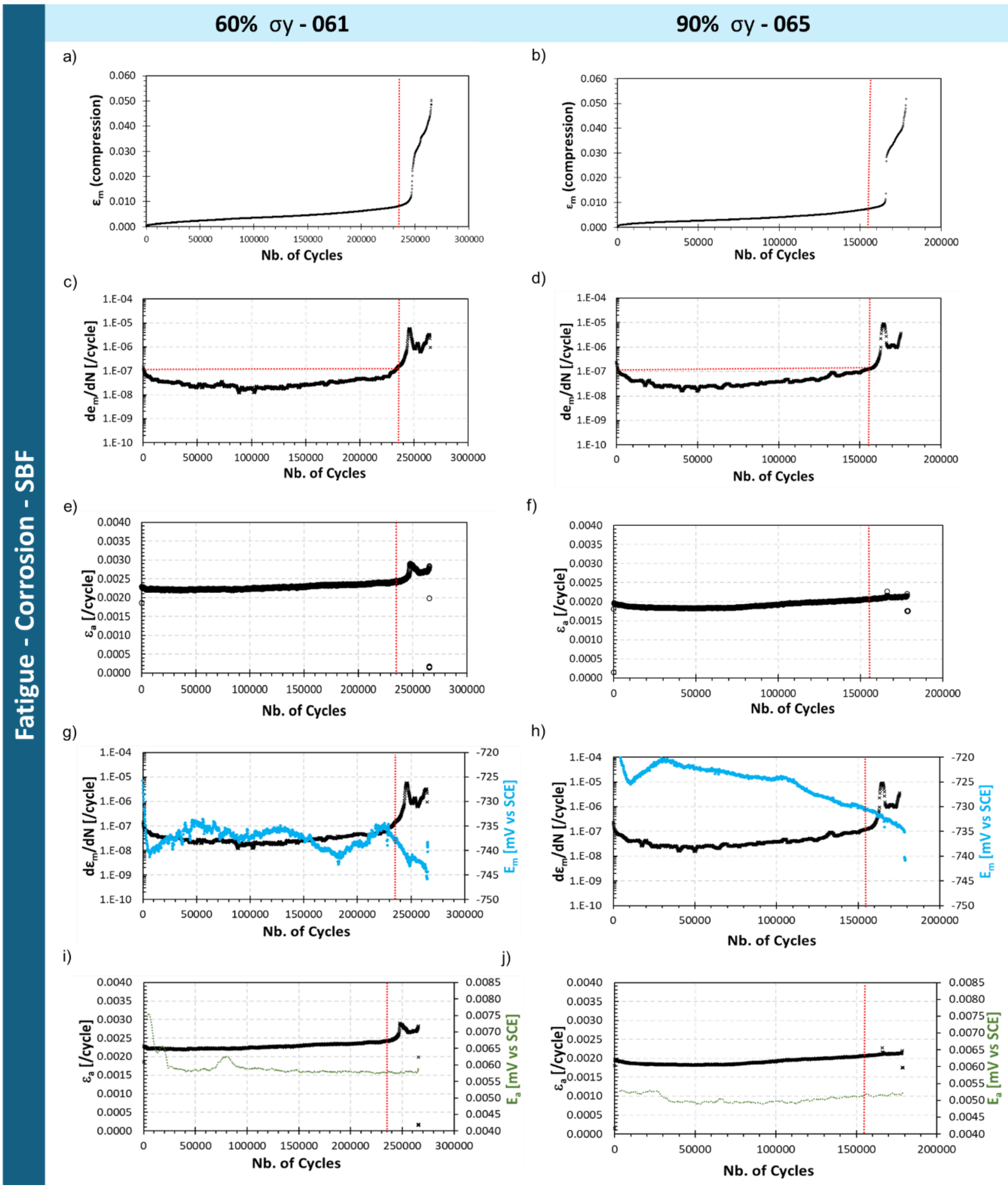

Figure 4.8 - Curves of Fe scaffolds under different conditions, in N_2: a) ε_m–N curve fatigue at 60% σ_y, b) ε_m–N curve fatigue at 90% σ_y, c) $d\varepsilon_m/dN$ vs N curve fatigue at 60% σ_y and d) $d\varepsilon_m/dN$ vs N curve fatigue at 90% σ_y e) ε_a–N curve fatigue at 60% σ_y, and f) b) ε_a–N curve fatigue at 90%. OCP responses during corrosion-fatigue: (g,h) differential strain rate vs. average potential; (i,j) strain amplitude vs. alternating potential at 60% and 90% of σ_y.

Figure 4.9 shows that specimens tested in a N_2 environment exhibit a longer fatigue life, reaching a significantly higher number of cycles for the same percentages of yield stress (σ_y) compared to those tested in SBF.

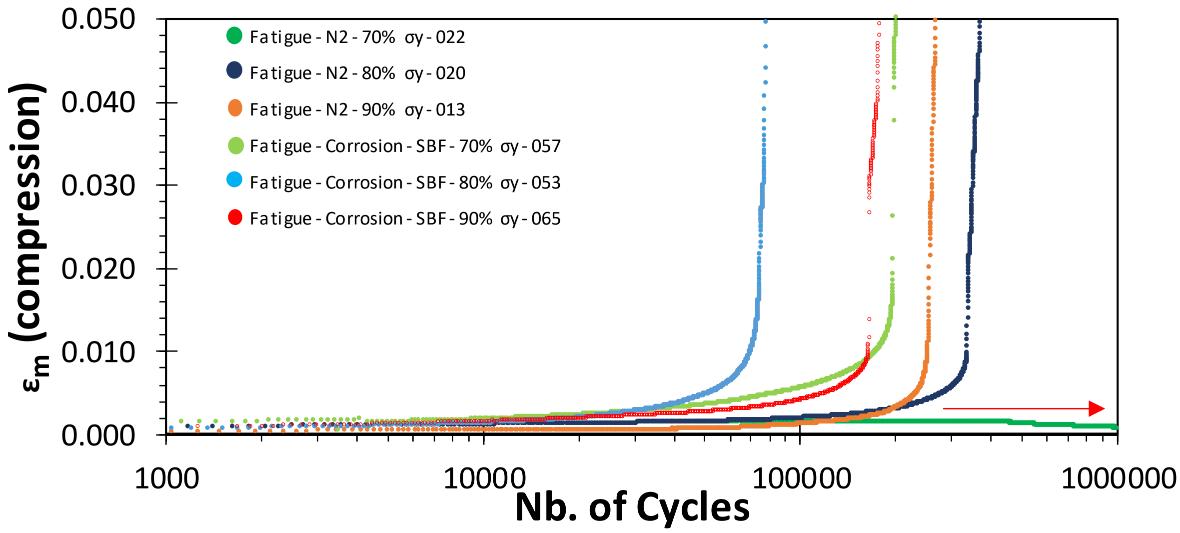

Figure 4.9 - Curves of Fe scaffolds, in N_2: and SBF, ε_m–N curve fatigue at 70%, 80% and 90% σ_y.

Figure 4.10 presents the Fast Fourier Transform (FFT) analysis of the corrosion potential (E_m) recorded during the axial corrosion-fatigue test performed at 60% of the σ_y in SBF. The FFT spectra were obtained at three distinct stages of the test at the beginning (10002 cycles), midway (100118 cycles), and near failure (260330 cycles) to evaluate the frequency response of the electrochemical signal throughout cyclic loading.

The analysis aimed to detect periodic components or harmonic fluctuations that could reveal electrochemical instabilities coupled with the mechanical loading frequency. However, no significant frequency shifts or new harmonic peaks were observed, indicating that the potential variations are primarily governed by the axial cyclic load and do not introduce additional oscillatory components.

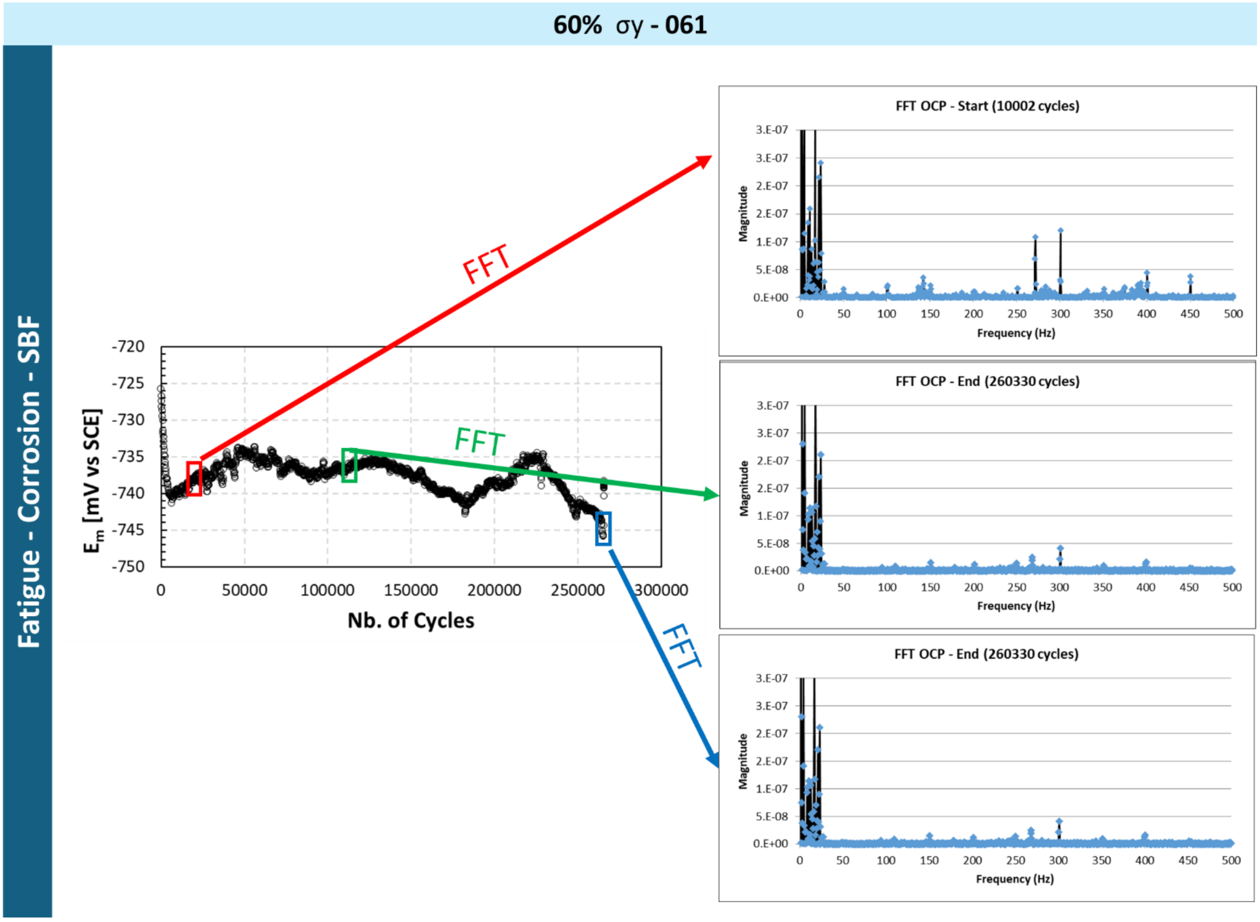

Figure 4.10 - FFT analysis of the corrosion potential signal obtained during the axial corrosion–fatigue test at 60% σ_Y in SBF.

Figure 4.11 shows that, in the tests performed in N_2, the classical fatigue behaviour is observed: as the fraction of σ_Y decreases, the number of cycles to failure increases, resulting in a longer fatigue life of the scaffold. Under corrosion-fatigue conditions, this trend is much more pronounced, being clear that corrosion is decreasing the life samples tested. In the 60–95% σ_Y interval, reducing the applied stress is not enough to increase considerably the life; instead, only a very limited variation in life is observed, indicating that lowering the load is not effective enough in improving durability in a corrosive environment. The presence of active corrosion during testing interfered with the scaffold's mechanical response, accelerating crack propagation. For the stress levels tested, in this case up to 60% σ_y, the life of the specimen is always limited showing that stress fatigue limit is far.

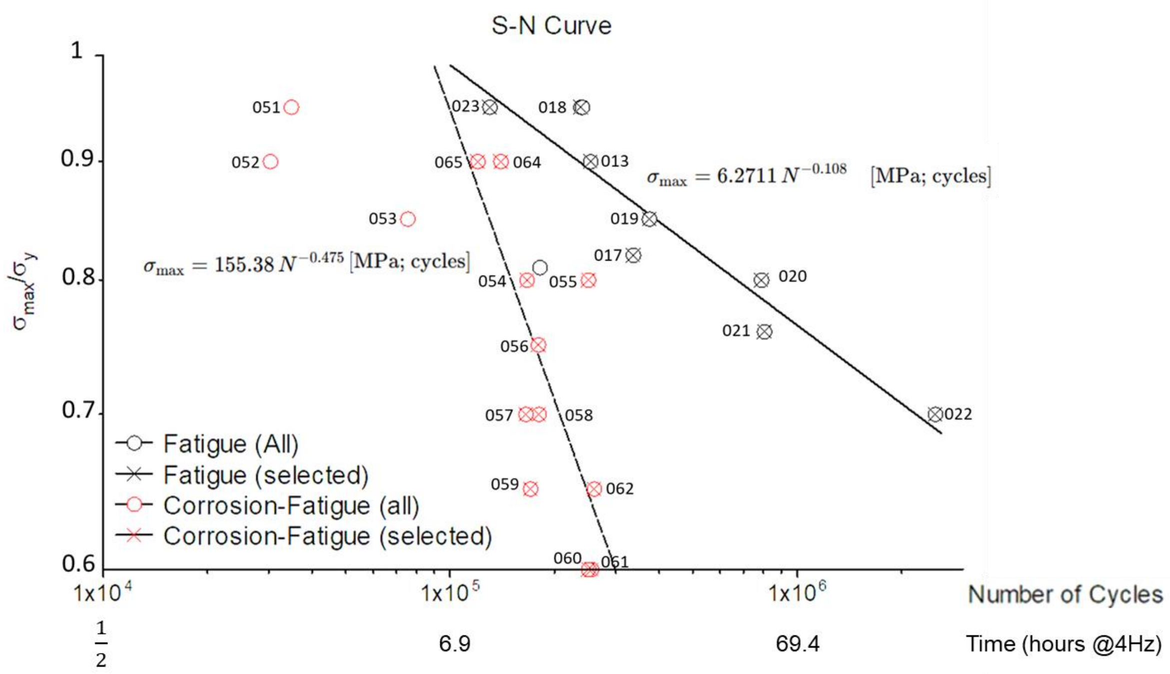

Figure 4.11 - Fatigue behaviour of AM Fe scaffold test specimens in N_2 and in SBF, S-N curve.

The Figure 4.12 show the 70% samples show different failure behaviours, with specimen 057 (corrosion-fatigue) deforming without complete fracture, while specimen 022 (fatigue) experienced full breakage after a large number of fatigue cycles; in contrast, the 75% samples (056 corrosion-fatigue and 021 fatigue) and the 90% samples (065 corrosion-fatigue and 013 fatigue) exhibit similar failure modes. Additional fracture-plane images for all specimens can be found in Appendix I. Another point is that all tests performed under fatigue revel a lot of struts that separate from the sample, something that was not observed for the specimens that were tested under corrosion-fatigue.

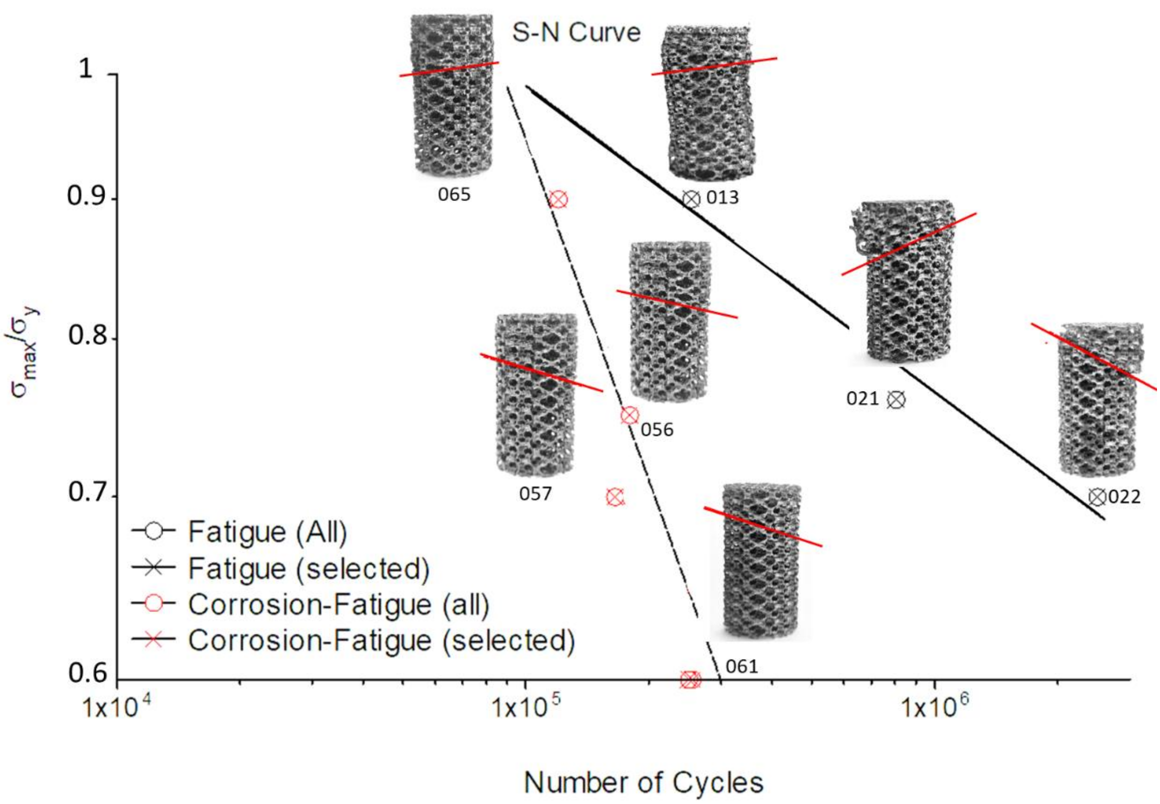

Figure 4.12 - S–N curve with the corresponding fractured samples, showing the fracture plane (red line) for each specimen.

Figure 4.13 presents the 3D reconstruction obtained by Micro-CT of an Fe scaffold after cyclic loading. In a), the overall architecture of the scaffold is shown, highlighting a unit cell located in the lower region that retains its structural integrity without visible signs of fatigue. Image b) displays the corresponding unit cell with RTCO geometry. Images c) and d) illustrate the deformation zones induced by fatigue and corrosion-fatigue, respectively. The regions marked in blue in d) indicate localized failure points, while the purple arrows highlight the reduction in height when comparing an undeformed cell with a deformed one—showing a decrease both in the overall cell height and in the individual struts. These changes occur mainly at the strut junctions on the right side of the scaffold, e). The struts tend to gradually deform by bending until fatigue fracture occurs, exhibiting partial fractures and shortening of the lateral arms, which indicates accumulated plastic deformation under repeated cyclic loading. The observed damage pattern confirms that fatigue consistently affects the same structural regions of the scaffold.

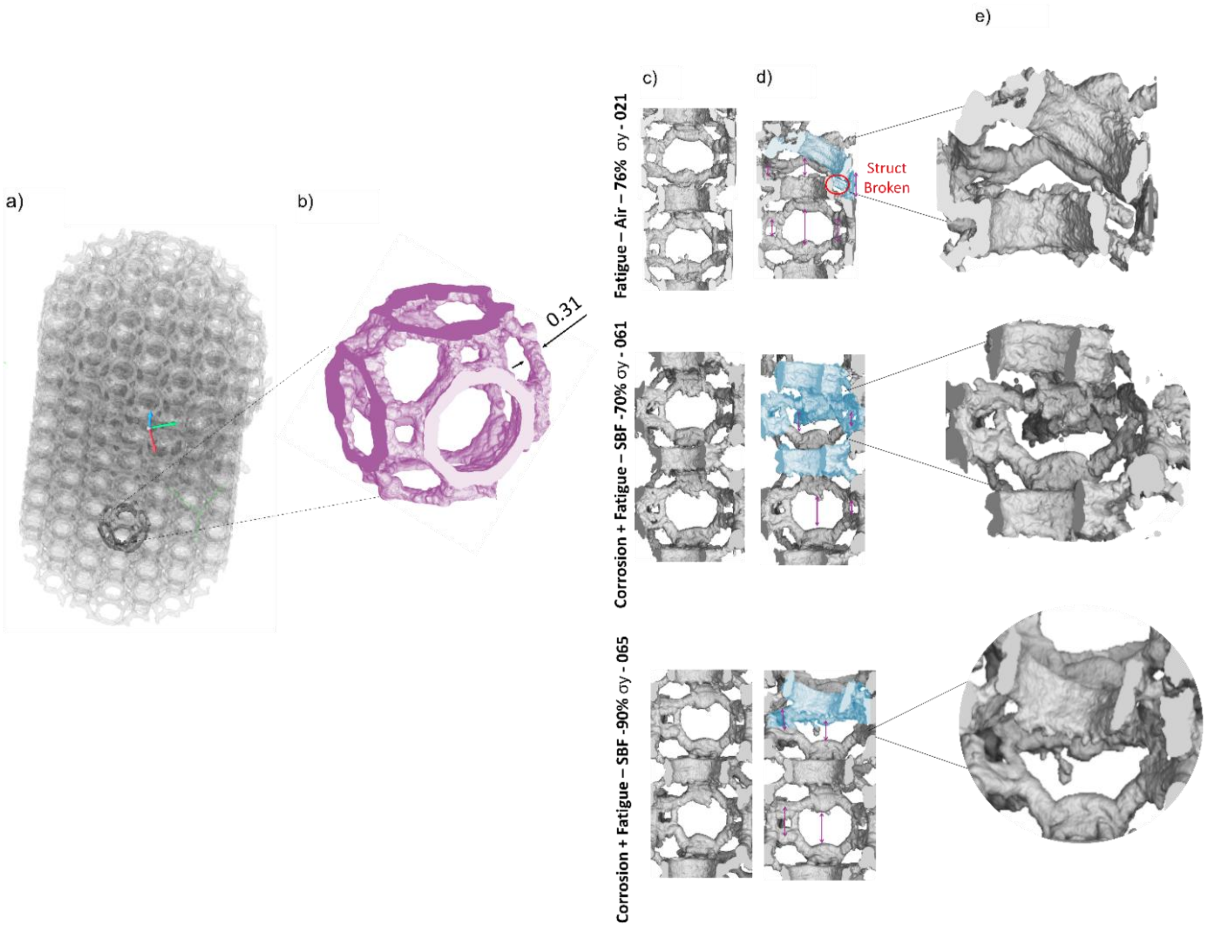

Figure 4.13 - Micro-CT reconstruction of an Fe scaffold after cyclic loading: a) overall scaffold geometry highlighting an intact unit cell; b) representative RTCO unit cell; c) localized deformation zones under fatigue in N_2; d)- e) deformation under corrosion-fatigue in SBF.

Figure 4.14 shows SEM micrographs of the Fe scaffold after cyclic loading tests in N_2 and in SBF corrosion-fatigue. At lower magnifications a) and d), the characteristic porous structure remains visible in both conditions. In the N_2 environment b), the red-marked region reveals clear strut fracture and brittle failure features, indicating localized stress concentration and crack propagation and the presence of a broken strut. Image c) highlights the specific failure point, with a surface fracture presenting a defect. In SBF corrosion-fatigue, the scaffold surface appears covered by corrosion products with a rough and porous morphology e), where the blue-marked regions correspond to corrosion products and corrosion film. Higher magnifications f) blue-marked areas again showing corrosion products, with EDS analysis confirms the presence of oxygen, phosphorus and calcium.

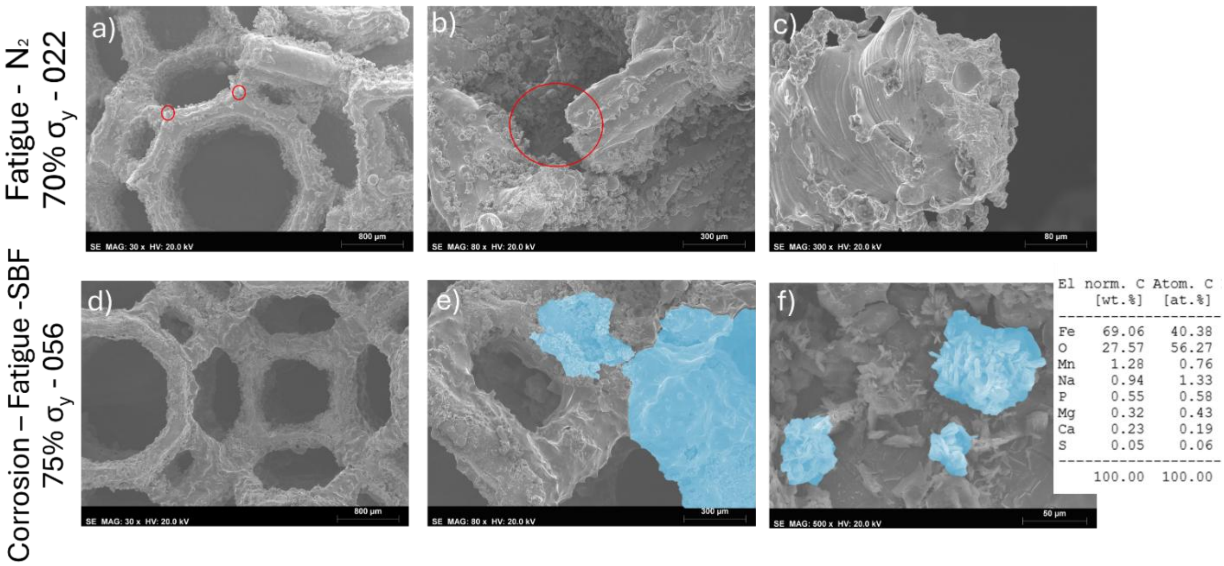

Figure 4.14 - SEM micrographs of the Fe scaffold after fatigue testing in N_2 (a-c) and in SBF (d – f).

Chapter 5

Discussion

The evolution observed in the OCP, in Figure 4.1, reflects the electrochemical dynamic interaction between the Fe surface and the SBF corrosive environment. The initial more negative potentials are associated with the direct exposure of Fe to the electrolyte, where oxidation reactions occur readily due to the absence of a protective film. The shift to more noble potential after 6 h suggests the initial formation of a surface film composed of corrosion products such as Fe oxides, hydroxides, and phosphates. This phenomenon results from the sequential oxidation of Fe to Fe^{2+}(Wackenrohr et al., 2022) and Fe^{3+} species in the physiological environment, followed by their reaction with hydroxyl ions generated from O_2 reduction. These reactions lead to the precipitation of compounds such as Fe-phosphates, forming a poorly soluble layer that temporarily hinders O_2 diffusion to the metal surface and reduces the corrosion rate (Li et al., 2019). The interaction of Fe ions with ionic species presents in SBF (Ca^{2+}, Cl^-, PO_4^{3-}, and OH^-) further promotes the consolidation of this partially protective film. This film temporarily reduces the corrosion rate, acting as a partial barrier to ion diffusion (Md Yusop et al., 2022).

The interaction of Fe ions with SBF constituents (Ca^{2+}, Cl^-, PO_4^{3-}, OH^-) further stabilizes this film through the formation of Ca and Fe phosphates and other mixed phases (Md Yusop et al., 2022) . However, with prolonged immersion time (1–7 days), the OCP gradually returns to more negative values, suggesting destabilization of the film and localized degradation, which reactivates metal dissolution. This degradation is exacerbated by Cl^-, which promote localized corrosion, and by the porosity and microstructural heterogeneity introduced by AM, which hinder uniform film formation and facilitate localized attack (Li et al., 2019; Wei et al., 2024).

For comparative purposes, the evolution of the OCP was analysed over 20 hours in SBF for both the Fe rod and the scaffold (Figure 4.2 a)), with similar behaviour observed in both: initially, the potential becomes more noble, followed by a phase of more pronounced instability in the rod, until, after a certain period, both converge to similar OCP values, stabilizing at around –750 mV after approximately 12 hours. In the fatigue-corrosion test (Figure 4.2 b), the same trend is observed, confirming the consistency of the electrochemical behaviour between the two conditions.

However, unlike the partial stabilization of the potential observed under corrosion conditions, the potential under fatigue exhibits more pronounced oscillations and an earlier tendency to decrease. This behaviour suggests that cyclic loading compromises the integrity of the corrosion product film, promoting its repeated rupture and the re-exposure of active Fe surface areas to the electrolyte. The mechanical stresses induced by fatigue seems to accelerate struts local corrosion and hinder the maintenance of a continuous protective barrier.

This behaviour confirms that corrosion fatigue in Fe alloys results from the interaction between mechanical damage and electrochemical instability. Even for smooth surfaces, the application of cyclic stresses makes the material vulnerable to localized degradation, as repeated mechanical deformation partially ruptures the film and re-exposes the metal to the electrolyte. The presence of aggressive ions, such as Cl^-, further intensifies this process by penetrating and destabilizing the protective layer, promoting pit nucleation and accelerating localized corrosion (Canut et al., 2019; Xu et al., 2022).

Under static conditions, the scaffold shows delayed and spatially heterogeneous, consistent with the mechanisms previously discussed for AM Fe (Li et al., 2019; Md Yusop et al., 2022). Although phosphate- and Ca-rich compounds can temporarily stabilize the surface (Wackenrohr et al., 2022), the film remains chemically unstable. Under cyclic loading, the structure exhibits less stable potential behaviour and earlier destabilization. The complex geometry amplifies stress concentration at the pore, weakening film adhesion and accelerating degradation (Canut et al., 2019) confirming the trend of previous results.

The electrochemical behaviour shown in Figure 4.4 reinforces and complements the trends previously identified through potential monitoring (Figure 4.1 to Figure 4.3). The low initial impedance and small semicircle diameter observed in the early stages of immersion are consistent with the negative OCP values reported in Figure 4.1, indicating a bare and electrochemically active Fe surface. The subsequent increase in impedance after 6 h is in line with the shift to more noble potentials, suggesting the formation of a transient film composed of Fe oxides and hydroxides, as discussed earlier (Huang et al., 2022; Md Yusop et al., 2022). After 24 h, the emergence of inductive behaviour and the flattening of the semicircle in the Nyquist plot correlate with the decline in OCP observed during prolonged immersion, confirming the onset of film destabilization and localized corrosion (Sim Sim Torres et al., 2021). This transition from a diffusion-controlled regime to one dominated by film relaxation and rupture processes supports the interpretation made in Figure 4.4 and Figure 4.1, where cyclic loading and geometric complexity were shown to accelerate the breakdown of the film and the reactivation of metal dissolution (Canut et al., 2019; W. C. Liu et al., 2025). Together, the impedance and potential data provide a coherent picture of the corrosion dynamics at the Fe–SBF interface, highlighting the temporal evolution from initial localized degradation and confirming the role of mechanical and morphological factors in modulating electrochemical stability.

Figure 4.5 presents Bode diagrams for the Fe rod a) and scaffold b), showing the temporal evolution of impedance modulus ($|Z|$) and phase angle (θ). For the Fe rod, an increase in $|Z|$ and θ after 6 h confirm film formation, consistent with OCP stabilization. After 24 h, a slight decline suggests partial film instability, but the system stabilizes at 72 and 168 h, maintaining high impedance values.

The analysis of the FTIR spectra (Figure 4.6 a)) obtained after 24 h of corrosion-fatigue testing confirms the formation of products typically observed in physiological environments, with characteristic bands attributed to hydroxyl, carbonate, and phosphate groups. The broad bands between 3600–3000 cm^{-1} (Gbenebor et al., 2017) and at 1628 cm^{-1} (Ling et al., 2017) correspond to the stretching and bending vibrations of the O–H group, associated with the presence of iron hydroxides and adsorbed water. The peak at 2875 cm^{-1} is related to C–H stretching vibrations (F. Liu et al., 2024) while the bands between 1368–1050 cm^{-1} (Ahmed et al., 2019) and at 877 cm^{-1} confirm the precipitation of carbonates and phosphates. The slight decrease in pH observed over 168 h of immersion (Figure 4.6 b)) reflects the progressive accumulation of corrosion products and the release of H^+ during redox reactions in SBF.

This trend confirms the chemical instability of the formed film and is consistent with the decrease in medium pH reported as a direct consequence of biodegradable iron degradation in physiological environments (Sharma & Pandey, 2019; Wackenrohr et al., 2022).

The analysis of fatigue tests revealed consistent structural behavior patterns in Fe scaffolds subjected to different stress levels and exposure environments N_2 (Figure 4.7) and SBF (Figure 4.8), highlighting the critical influence of cyclic loading and biodegradation on the material's functional durability. In SBF, the fatigue life of Fe scaffolds until yielding is significantly shorter than in N_2, due to the synergistic action between mechanical fatigue and electrochemical degradation. Recent studies reinforce that corrosion-fatigue governs the failure process, accelerating crack nucleation and compromising structural integrity from the earliest loading cycles (Canut et al., 2019; Li et al., 2019; Ordnung et al., 2025; Simões et al., 2022).

The evolution of the ε_m–N and $d\varepsilon_m/dN$–N curves provide further insight into damage progression under cyclic loading. While the ε_m–N curves show a gradual increase in mean strain followed by a sharp rise near failure, the derivative curve $d\varepsilon_m/dN$–N offers a more sensitive response to microstructural changes, with a distinct inflection point preceding macroscopic yielding. Among the evaluated thresholds, the 1×10^{-7} criterion in the $d\varepsilon_m/dN$–N curve anticipates the moment when the material ceases to respond elastically in a stable manner, indicating the onset of significant internal changes in the microstructure, even before visible strain localization occurs. This early deviation in the curve's behavior suggests that crack nucleation and stiffness loss mechanisms are already active, although not yet evident in the macroscopic strain distribution. This early variation correlates with crack initiation and structural stiffness degradation, as confirmed by the Em–N trend, which shows a progressive reduction in E. Additionally, the ε_a/N ratio remains relatively stable until the damage threshold is reached, after which it increases abruptly, indicating a shift in the deformation mode. Taken together, these indicators demonstrate that the 1×10^{-7} threshold in the $d\varepsilon_m/dN$–N curve is the most reliable and reproducible criterion for early damage detection in Fe scaffolds subjected to fatigue loading, especially in corrosive environments.

As shown in Figure 4.8, for equivalent stress levels (60% or 90% of σ_Y), scaffolds tested in SBF reach failure after fewer cycles than those tested in N_2 (Figure 4.7). This reduction in fatigue life is explained by corrosion-fatigue mechanisms, in which the simulated physiological environment accelerates material degradation through three main pathways: cyclic rupture of the film, which repeatedly exposes the metallic surface to aggressive ions such as Cl^- and PO_4^{3-} (Putra et al., 2024) stress concentration at strut junctions, identified as critical areas where the combined action of tensile stress and chemical attack promotes premature failure (Canut et al., 2019); and the loss of a fatigue limit in corrosive environments, where the number of cycles to failure becomes governed by the corrosion rate rather than by the applied stress.

The S–N curve obtained (Figure 4.11) further reinforces these findings, revealing clear differences between fatigue behaviour in N_2 and in SBF. In N_2, Fe scaffolds follow the classical fatigue trend: as the applied stress decreases, the number of cycles to failure increases (Simões et al., 2022). In contrast, tests performed in SBF show that applied stress has a limited influence on fatigue life, indicating that corrosion dominates the failure mechanism and accelerates crack nucleation. Similar behaviour has been reported for porous Fe scaffolds produced by selective laser melting, where corrosion-driven damage suppresses the classical mechanical fatigue response (Wackenrohr et al., 2022).

Electrochemical degradation in SBF is sufficiently aggressive to cause structural yielding even at lower stress levels (Schumacher et al., 2024). Studies on FeMn alloys also show that localized corrosion, rather than mechanical loading, becomes the primary factor limiting scaffold longevity (Putra et al., 2024). At higher testing frequencies, the influence of corrosion becomes less pronounced, as the shorter exposure time per cycle reduces electrochemical attack, allowing the classical fatigue trend to become more evident. These comparisons highlight that both loading frequency and environment critically modulate the interaction between mechanical and chemical damage in biodegradable Fe scaffolds (Li et al., 2019).

In SBF, the initial formation of a crack or surface defect triggers the temporary development of a film composed of Fe oxides, which provides only short-term protection. Under cyclic loading, this film is repeatedly ruptured, re-exposing the metallic substrate to the aggressive medium. This continuous cycle of film formation and breakdown accelerates localized corrosion (Wackenrohr et al., 2022).

Based on the Ashby model relationships, the mechanical response of the scaffold was positioned on the diagram through the calculation of the relative modulus and the relative yield stress: with an $E_{scaffold}$ of 0.56 GPa and an E_{bulk} of 171.70 GPa, a value that is slightly lower than the expected for this type of metallic material, which should be close to 200 GPa, a relative modulus of $\frac{E}{Es} \approx 0.00326$ was obtained (bulk properties were determined from a compressive tests that as carried on to this material). Considering a σ_Y of 2.78 MPa for the scaffold and 432.86 MPa for the bulk material, the relative σ_Y is $\frac{\sigma y}{\sigma ys} \approx 0.0064$. With a relative density of $\frac{\rho}{\rho s} = 0.10$ (10% density), these values place the structure in Figure 5.1 a) and b) close to the bending-dominated regime. These curves were generated using MATLAB, based on the theoretical scaling laws defined by the Ashby model (Ashby, 2006).

This framework helps justify the behaviour observed in the S–N curves in SBF, where the scaffolds exhibit a lower number of cycles to failure, meaning a significantly shorter fatigue life. In a bending-dominated regime, the load is mainly supported through strut bending and stress concentration at the junctions, making the structure mechanically less efficient, more sensitive to geometric imperfections, and substantially more vulnerable to corrosion. Thus, the combination of bending-dominated behaviour and corrosive degradation accelerates crack nucleation and propagation, explaining the pronounced reduction in fatigue durability observed in the SBF environment.

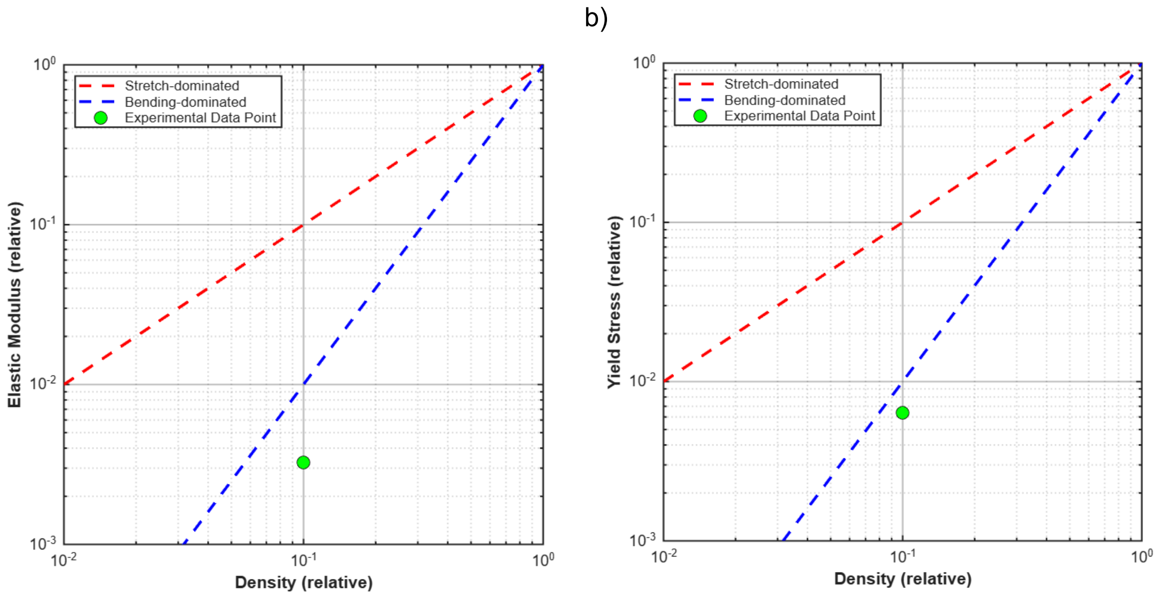

Figure 5.1 - Relative mechanical properties of the Fe RTCO: a) Relative elastic modulus, and b) Relative yield stress in function of the relative density.

This behavior is corroborated by structural analyses performed using micro-CT (Figure 4.13), which systematically demonstrated that fracture occurs preferentially at the junctions of scaffold struts, regardless of the applied stress level. This spatial recurrence of failure suggests that these regions act as critical zones of stress concentration and localized degradation, making them particularly vulnerable to the combined effects of cyclic loading and corrosion. Micro-CT analysis (Figure 4.13) revealed that fracture consistently initiated at the strut junctions, while SEM observations (Figure 4.14) identified corrosion products rich in Fe oxides and phosphates adhering to the internal surfaces after exposure to SBF. These findings demonstrate that the junctions act as critical regions of stress concentration and localized corrosion, leading to recurrent fracture and accelerated crack propagation. Similar results have been reported in the literature, confirming that failure predominantly occurs at these junctions and is closely associated with the accumulation of corrosion products on the surface (Kumar et al., 2025; Putra et al., 2024; Zhao et al., 2022).

From these results, it is confirmed that Ashby can also be applied to these materials, revealing that the prediction corresponds to what of observed in the samples tested.

Chapter 6

Conclusion and Future Work

This study evaluated the corrosion, fatigue, and corrosion-fatigue behaviour of porous iron scaffolds produced by AM, based on RTCO unit cells, under conditions simulating a physiological environment. The results revealed the strong interdependence between electrochemical and mechanical mechanisms in the degradation of these materials.

During corrosion tests, an initial formation of layer of oxides, hydroxides, and Fe phosphates was observed on the surface, temporarily reducing the corrosion rate. Over time, this layer lost stability due to chloride ions in the medium, leading to localized corrosion and reactivation of metal dissolution. This degradation process reflects the limited protectiveness and transient nature of corrosion product film. Electrochemical analysis confirmed this process through variations in impedance and potential behaviour.

Fatigue tests under compression-compression and inert conditions showed stable cyclic behaviour with localized deformation at the strut junctions. However, under corrosion-fatigue conditions, cyclic loading caused repeated rupture of the corrosion film, accelerating degradation. The analysis of the S–N curve clearly highlights the differences between fatigue behaviour in inert and physiological environments. In nitrogen, the Fe scaffolds follow the classical fatigue response, with the number of cycles to failure increasing as the applied stress decreases, and a fatigue limit is reached at around 1×10^7 cycles, close to 70% of the yield strength. In contrast, under SBF conditions the fatigue life is drastically reduced due to the synergistic effect of corrosion and fatigue, and no clear fatigue limit is observed, indicating that electrochemical degradation dominates the failure mechanism in the corrosive environment.

Furthermore, by observing the micro-CT of the damage scaffold and from SEM imagens of some broken struts, it was found that the failure occurs mainly at the strut junctions by bending loads, also confirmed by Ashby model, revealing that this model can be also applied to these scaffolds.

Chemical analyses (SEM/EDS) confirmed the presence of Fe, O, P and Ca elements, typical of phosphate and oxide corrosion products. The detection of these species indicates the coexistence of iron oxides and calcium phosphates formed through ion exchange reactions with SBF constituents. Morphological analyses confirmed that fracture consistently occurs at strut junctions, identified as stress concentration regions of stress concentration and localized attack. Overall, corrosion-fatigue was identified as the main degradation mechanism, leading to premature failure. The synergistic interaction between electrochemical instability and cyclic mechanical loading accelerates both crack initiation and propagation. Despite this, the RTCO porous iron scaffolds demonstrated significant potential as biodegradable biomaterials for bone regeneration, if degradation is controlled. In this case, due to the versability of the additive manufacturing, the density of the scaffolds can be easily changed to control the degradation rate and fatigue response, in order to develop scaffolds for patient specific needs.

Future work should focus on improving corrosion resistance and biological performance through protective coatings and surface functionalization, aiming to promote uniform corrosion and mechanical stability. The application of composite coatings, such as biodegradable polymers (PLGA, PCL) with bioactive ceramics (hydroxyapatite), can act as temporary barriers that control the corrosion rate, reduce localized attacks, and enhance biocompatibility. Additionally, in vitro biological studies on cell adhesion, proliferation, and differentiation are essential to deepen the understanding of scaffold–tissue interactions and to develop optimized biodegradable implants for BR.

Bibliography

Additive manufacturing-General principles- ISO/ASTM 52900. (2021).

Ahmed, A. A., Gypser, S., Leinweber, P., Freese, D., & Kühn, O. (2019). Infrared spectroscopic characterization of phosphate binding at the goethite-water interface. *Physical Chemistry Chemical Physics*, *21*(8), 4421–4434. https://doi.org/10.1039/c8cp07168c

Ashby, M. F. (2006). The properties of foams and lattices. *Philosophical Transactions of the Royal Society A: Mathematical, Physical and Engineering Sciences*, *364*(1838), 15–30. https://doi.org/10.1098/rsta.2005.1678

Avdeev, Y. G., & Kuznetsov, Y. I. (2023). Iron oxide and oxyhydroxide phases formed on steel surfaces and their dissolution in acidic media. Review*. In *International Journal of Corrosion and Scale Inhibition* (Vol. 12, Issue 2, pp. 366–409). Russian Association of Corrosion Engineers. https://doi.org/10.17675/2305-6894-2023-12-2-1

Bahrudin, M. T. A. H., Januddi, F. S., Sarian, M. N., Arafat, A., Nur, H., & Md Yusop, A. H. (2025). Current status of additively manufactured porous Fe-based scaffolds for bone applications: A review from design, corrosion and biocompatibility viewpoints. In *Materials Today Communications* (Vol. 42). Elsevier Ltd. https://doi.org/10.1016/j.mtcomm.2024.111247

Bayram, F., Göçmen, G., & Özkan, Y. (2024). Evaluating risk factors and complications in mandibular ramus block grafting: a retrospective cohort study. *Clinical Oral Investigations*, *28*(4). https://doi.org/10.1007/s00784-024-05613-6

Cammarata, A., & Mastropasqua, L. (2023). Theoretical analysis of mixed open-circuit potential for high temperature electrochemical cells electrodes. *Frontiers in Energy Research*, *11*. https://doi.org/10.3389/fenrg.2023.1120343

Canut, F. A., Simões, A. M. P., Reis, L., Freitas, M., Bastos, I. N., Castro, F. C., & Mamiya, E. N. (2019). Monitoring of corrosion-fatigue degradation of grade R4 steel using an electrochemical-mechanical combined approach. *Fatigue and Fracture of Engineering Materials and Structures*, *42*(11), 2509–2519. https://doi.org/10.1111/ffe.13079

Dong, H., Lin, F., Boccaccini, A. R., & Virtanen, S. (2021). Corrosion behavior of biodegradable metals in two different simulated physiological solutions: Comparison of Mg, Zn and Fe. *Corrosion Science*, *182*. https://doi.org/10.1016/j.corsci.2021.109278

Fagali, N. S., Madrid, M. A., Pérez MacEda, B. T., López Fernández, M. E., Lozano Puerto, R. M., & De Mele, M. F. L. (2020). Effect of degradation products of iron-bioresorbable implants on the physiological behavior of macrophages: In vitro. *Metallomics*, *12*(11), 1841–1850. https://doi.org/10.1039/d0mt00151a

Feng, J., Liu, J., Wang, Y., Diao, J., Kuang, Y., & Zhao, N. (2023). Beta-TCP scaffolds with rationally designed macro-micro hierarchical structure improved angio/osteo-genesis capability for bone regeneration. *Journal of Materials Science: Materials in Medicine*, *34*(7). https://doi.org/10.1007/s10856-023-06733-3

Francis, A. P., Augustus, A. R., Chandramohan, S., Bhat, S. A., Priya, V. V., & Rajagopalan, R. (2023).

A review on biomaterials-based scaffold: An emerging tool for bone tissue engineering. *Materials Today Communications*, *34*. https://doi.org/10.1016/j.mtcomm.2022.105124

Freitas, M., Reis, L., Li, B., Guelho, I., Antunes, V., Maia, J., & Cláudio, R. A. (2014). In-plane biaxial fatigue testing machine powered by linear iron-core motors. *ASTM Special Technical Publication*, *STP 1571*, 63–79. https://doi.org/10.1520/STP157120130078

Gąsior, G., Szczepański, J., & Radtke, A. (2021). Biodegradable iron-based materials—what was done and what more can be done? In *Materials* (Vol. 14, Issue 12). MDPI AG. https://doi.org/10.3390/ma14123381

Gbenebor, O. P., Adeosun, S. O., Lawal, G. I., Jun, S., & Olaleye, S. A. (2017). Acetylation, crystalline and morphological properties of structural polysaccharide from shrimp exoskeleton. *Engineering Science and Technology, an International Journal*, *20*(3), 1155–1165. https://doi.org/10.1016/j.jestch.2017.05.002

Global Bone Marrow Market. (2020).

Gorejová, R., Haverová, L., Oriňaková, R., Oriňak, A., & Oriňak, M. (2019). Recent advancements in Fe-based biodegradable materials for bone repair. In *Journal of Materials Science* (Vol. 54, Issue 3, pp. 1913–1947). Springer New York LLC. https://doi.org/10.1007/s10853-018-3011-z

Herrera Hernández, H., M. Ruiz Reynoso, A., C. Trinidad González, J., O. González Morán, C., G. Miranda Hernández, J., Mandujano Ruiz, A., Morales Hernández, J., & Orozco Cruz, R. (2020). Electrochemical Impedance Spectroscopy (EIS): A Review Study of Basic Aspects of the Corrosion Mechanism Applied to Steels. In *Electrochemical Impedance Spectroscopy*. IntechOpen. https://doi.org/10.5772/intechopen.94470

Huang, J., Voigt, M., Wackenrohr, S., Ebbert, C., Keller, A., Maier, H. J., & Grundmeier, G. (2022). Influence of hydrogel coatings on corrosion and fatigue of iron in simulated body fluid. *Materials and Corrosion*, *73*(7), 1034–1044. https://doi.org/10.1002/maco.202112841

Jang, J. W., Min, K. E., Kim, C., Shin, J., Lee, J., & Yi, S. (2023). Review: Scaffold Characteristics, Fabrication Methods, and Biomaterials for the Bone Tissue Engineering. In *International Journal of Precision Engineering and Manufacturing* (Vol. 24, Issue 3, pp. 511–529). SpringerOpen. https://doi.org/10.1007/s12541-022-00755-7

Kalva, S. N., Zakaria, Y., Velasquez, C. A., & Koç, M. (2025). Tailoring the mechanical and degradation properties of 3DP PLA/PCL scaffolds for biomedical applications. *Reviews on Advanced Materials Science*, *64*(1). https://doi.org/10.1515/rams-2025-0098

Kokubo, T., & Takadama, H. (2006). How useful is SBF in predicting in vivo bone bioactivity? *Biomaterials*, *27*(15), 2907–2915. https://doi.org/10.1016/j.biomaterials.2006.01.017

Kontakis, M. G., Moulin, M., Andersson, B., Norein, N., Samanta, A., Stelzl, C., Engberg, A., Diez-Escudero, A., Kreuger, J., & Hailer, N. P. (2025). Trabecular-bone mimicking osteoconductive collagen scaffolds: an optimized 3D printing approach using freeform reversible embedding of suspended hydrogels. *3D Printing in Medicine*, *11*(1). https://doi.org/10.1186/s41205-025-00255-0

Kumar, A., Yadav, M., & Sharma, P. (2025). Biodegradable iron–hydroxyapatite scaffolds fabricated via advanced rapid tooling: unveiling mechanical properties, corrosion behaviour, and biocompatibility. *Progress in Additive Manufacturing*. https://doi.org/10.1007/s40964-025-01133-1

Lai, R., Jiang, J., Huo, Y., Wang, H., Bosiakov, S., Lyu, Y., & Li, L. (2025). Design of novel graded bone scaffolds based on triply periodic minimal surfaces with multi-functional pores. *Frontiers in Bioengineering and Biotechnology*, *13*. https://doi.org/10.3389/fbioe.2025.1503582

Laubach, M., Whyte, S., Chan, H. F., Frankenbach-Désor, T., Mayer-Wagner, S., Hildebrand, F., Holzapfel, B. M., Kneser, U., Dulleck, U., & Hutmacher, D. W. (2024). Lost in translation: the lack of agreement between surgeons and scientists regarding biomaterials research and innovation for treating bone defects. *BMC Medicine*, *22*(1). https://doi.org/10.1186/s12916-024-03734-z

Lee, S. S., Du, X., Kim, I., & Ferguson, S. J. (2022). Scaffolds for bone-tissue engineering. In *Matter* (Vol. 5, Issue 9, pp. 2722–2759). Cell Press. https://doi.org/10.1016/j.matt.2022.06.003

Li, Y., Jahr, H., Lietaert, K., Pavanram, P., Yilmaz, A., Fockaert, L. I., Leeflang, M. A., Pouran, B., Gonzalez-Garcia, Y., Weinans, H., Mol, J. M. C., Zhou, J., & Zadpoor, A. A. (2018). Additively manufactured biodegradable porous iron. *Acta Biomaterialia*, *77*, 380–393. https://doi.org/10.1016/j.actbio.2018.07.011

Li, Y., Lietaert, K., Li, W., Zhang, X. Y., Leeflang, M. A., Zhou, J., & Zadpoor, A. A. (2019). Corrosion fatigue behavior of additively manufactured biodegradable porous iron. *Corrosion Science*, *156*, 106–116. https://doi.org/10.1016/j.corsci.2019.05.003

Lin, C. Y., & Kang, J. H. (2021). Mechanical properties of compact bone defined by the stress-strain curve measured using uniaxial tensile test: A concise review and practical guide. In *Materials* (Vol. 14, Issue 15). MDPI AG. https://doi.org/10.3390/ma14154224

Ling, F. T., Post, J. E., Heaney, P. J., Kubicki, J. D., & Santelli, C. M. (2017). Fourier-transform infrared spectroscopy (FTIR) analysis of triclinic and hexagonal birnessites. *Spectrochimica Acta - Part A: Molecular and Biomolecular Spectroscopy*, *178*, 32–46. https://doi.org/10.1016/j.saa.2017.01.032

Liu, F., Liu, Y., Guo, Y., Liu, J., Dong, J., Wang, T., Hao, D., & Zhang, Y. (2024). FTIR determination of the degree of molar substitution for hydroxypropyl chitosan. *Carbohydrate Polymers*, *339*. https://doi.org/10.1016/j.carbpol.2024.122229

Liu, W. C., Chang, H. W., Huang, S. I., Yang, K. Y., Tsai, P. I., Chen, C. H., Wang, Y. H., Ma, C. H., Chen, C. Y., & Fu, Y. C. (2025). Biodegradable porous iron versus titanium interference screws in porcine ACL reconstruction model: a one-year observational study. *Npj Materials Degradation*, *9*(1). https://doi.org/10.1038/s41529-025-00602-w

Liu, Y., Ren, D., Li, S., Wang, H., Zhang, L., & Sercombe, T. (n.d.). *Enhanced fatigue characteristics of topologically optimized biomedical titanium porous structure by selective laser melting*.

Lozhkomoev, A. S., Buyakov, A. S., Kazantsev, S. O., Senkina, E. I., Krinitcyn, M. G., Ivanyuk, V. A., Sharipova, A. F., & Lerner, M. I. (2022). Preparation and Properties of Iron Nanoparticle-Based Macroporous Scaffolds for Biodegradable Implants. *Materials*, *15*(14). https://doi.org/10.3390/ma15144900

Łuczak, J. W., Palusińska, M., Matak, D., Pietrzak, D., Nakielski, P., Lewicki, S., Grodzik, M., & Szymański, Ł. (2024). The Future of Bone Repair: Emerging Technologies and Biomaterials in Bone Regeneration. In *International Journal of Molecular Sciences* (Vol. 25, Issue 23). Multidisciplinary Digital Publishing Institute (MDPI). https://doi.org/10.3390/ijms252312766

Md Yusop, A. H., Al Sakkaf, A., & Nur, H. (2022). Modifications on porous absorbable Fe-based scaffolds for bone applications: A review from corrosion and biocompatibility viewpoints. In *Journal of Biomedical Materials Research - Part B Applied Biomaterials* (Vol. 110, Issue 1, pp. 18–44). John Wiley and Sons Inc. https://doi.org/10.1002/jbm.b.34893

Mukasheva, F., Adilova, L., Dyussenbinov, A., Yernaimanova, B., Abilev, M., & Akilbekova, D. (2024). Optimizing scaffold pore size for tissue engineering: insights across various tissue types. In *Frontiers in Bioengineering and Biotechnology* (Vol. 12). Frontiers Media SA. https://doi.org/10.3389/fbioe.2024.1444986

Noordin, M. A., Md Yusop, A. H., Syahrom, A., & Md Saad, A. P. (2025). Mechanistic Analysis of Porous Iron Scaffold Degradation in Cancellous Bone Structure Subjected to Dynamic Simulated Body Fluid. *Journal of Bionic Engineering*, *22*(1), 306–321. https://doi.org/10.1007/s42235-024-00628-x

Ordnung, D., Sinico, M., Mertens, T., Haitjema, H., & Van Hooreweder, B. (2025). Enhancing Fatigue Life of Metal Parts Produced by High-Speed Laser Powder Bed Fusion Through In Situ Surface Quality Improvement. *Journal of Manufacturing and Materials Processing*, *9*(7). https://doi.org/10.3390/jmmp9070207

Patel, M. V., Cudjoe, E., & Ryu, J. J. (2024). Sliding Contact Fatigue Damage of Metallic Implants in a Simulated Body Fluid Environment. *Lubricants*, *12*(12). https://doi.org/10.3390/lubricants12120437

Percival, K. M., Paul, V., & Husseini, G. A. (2024). Recent Advancements in Bone Tissue Engineering: Integrating Smart Scaffold Technologies and Bio-Responsive Systems for Enhanced Regeneration. In *International Journal of Molecular Sciences* (Vol. 25, Issue 11). Multidisciplinary Digital Publishing Institute (MDPI). https://doi.org/10.3390/ijms25116012

Perier-Metz, C., Duda, G. N., & Checa, S. (2021). Initial mechanical conditions within an optimized bone scaffold do not ensure bone regeneration – an in silico analysis. *Biomechanics and Modeling in Mechanobiology*, *20*(5), 1723–1731. https://doi.org/10.1007/s10237-021-01472-2

Prakoso, A. T., Ichsan, A. R., Syahrom, A., Md Saad, A. P., Wahab, A. H. A., Sulong, M. A., Ghazali, F. A. M., & Basri, H. (2020). Mechanical Degradation Model of Porous Fe Scaffold: Simulation Approach. *Journal of Physics: Conference Series*, *1500*(1). https://doi.org/10.1088/1742-6596/1500/1/012023

Putra, N. E., Moosabeiki, V., Leeflang, M. A., Zhou, J., & Zadpoor, A. A. (2024). Biodegradation-affected fatigue behavior of extrusion-based additively manufactured porous iron–manganese scaffolds. *Acta Biomaterialia*, *178*, 340–351. https://doi.org/10.1016/j.actbio.2024.02.024

Ramaglia Amadasi, R., Rogati, G., Liverani, E., Leardini, A., & Caravaggi, P. (2025). An integrated experimental and analytical approach for the analysis of the mechanical interaction between metal porous scaffolds and bone: implications for stress shielding in orthopedic implants. *Frontiers in Bioengineering and Biotechnology*, *13*. https://doi.org/10.3389/fbioe.2025.1562367

Rasheed, S., Lughmani, W. A., Khan, M. M., Brabazon, D., Obeidi, M. A., & Ahad, I. U. (2023). The Porosity Design and Deformation Behavior Analysis of Additively Manufactured Bone Scaffolds through Finite Element Modelling and Mechanical Property Investigations. *Journal of Functional Biomaterials*, *14*(10). https://doi.org/10.3390/jfb14100496

Renishaw. (2025). *VIONiC^{TM} incremental optical encoder system data sheet*. www.renishaw.com/vionicdownloads

Rezapourian, M., Kamboj, N., Jasiuk, I., & Hussainova, I. (2022). Biomimetic design of implants for long bone critical-sized defects. *Journal of the Mechanical Behavior of Biomedical Materials*, *134*. https://doi.org/10.1016/j.jmbbm.2022.105370

Sakkaf, A. Al, Januddi, F. S., Yusop, A. H. M., & Nur, H. (2022). Challenges in the use of Fe-based materials for bone scaffolds applications: Perspective from in vivo biocorrosion. In *Materials Today Communications* (Vol. 33). Elsevier Ltd. https://doi.org/10.1016/j.mtcomm.2022.104564

Salama, M., Vaz, M. F., Colaço, R., Santos, C., & Carmezim, M. (2022). Biodegradable Iron and Porous Iron: Mechanical Properties, Degradation Behaviour, Manufacturing Routes and Biomedical Applications. *Journal of Functional Biomaterials*, *13*(2). https://doi.org/10.3390/jfb13020072

Salari, N., Darvishi, N., Bartina, Y., Larti, M., Kiaei, A., Hemmati, M., Shohaimi, S., & Mohammadi, M. (2021). Global prevalence of osteoporosis among the world older adults: a comprehensive systematic review and meta-analysis. In *Journal of Orthopaedic Surgery and Research* (Vol. 16, Issue 1). BioMed Central Ltd. https://doi.org/10.1186/s13018-021-02821-8

Sarian, M. N., Iqbal, N., Sotoudehbagha, P., Razavi, M., Ahmed, Q. U., Sukotjo, C., & Hermawan, H. (2022). Potential bioactive coating system for high-performance absorbable magnesium bone implants. In *Bioactive Materials* (Vol. 12, pp. 42–63). KeAi Communications Co. https://doi.org/10.1016/j.bioactmat.2021.10.034

Schulze, F., Lang, A., Schoon, J., Wassilew, G. I., & Reichert, J. (2023). Scaffold Guided Bone Regeneration for the Treatment of Large Segmental Defects in Long Bones. In *Biomedicines* (Vol. 11, Issue 2). MDPI. https://doi.org/10.3390/biomedicines11020325

Schumacher, L., Cetin, I. N., Bielefeldt, S., Rupp, F., & Roehler, A. (2024). Enhanced Experimental Setup and Methodology for the Investigation of Corrosion Fatigue in Metallic Biodegradable Implant Materials. *Materials*, *17*(21). https://doi.org/10.3390/ma17215146

Sharma, P., & Pandey, P. M. (2019). Corrosion behaviour of the porous iron scaffold in simulated body fluid for biodegradable implant application. *Materials Science and Engineering C*, *99*, 838–852. https://doi.org/10.1016/j.msec.2019.01.114

Shen, N., Zhang, Z., Wu, F., Zhu, Z., Liu, J., Qi, X., Li, Q., Wang, X., Ma, Q., & Xiang, H. (2025). Advances in self-powered biomaterials for bone defect repair. In *Advanced Composites and Hybrid Materials* (Vol. 8, Issue 1). Springer Science and Business Media B.V. https://doi.org/10.1007/s42114-024-01115-x

Sim Sim Torres, E., Carlos Salvador Santos Fernandes Dalila Madeira Nascimento Mil-Homens Júri Presidente, J., Paulo Sequeira Farinha Orientador, J., Carlos Salvador Santos Fernandes Vogal, J., & Teresa Oliveira de Moura Silva, M. (2021). *Dissertação Revestimentos Inorgânicos para Ligas de Magnésio Usadas em Implantes Ortopédicos Engenharia de Materiais*.

Simões, A. M. P., Canut, F. A., Reis, ; L, Bastos, ; I N, & Mamiya, ; E N. (2022). *CP4 ELECTROCHEMICAL ASSESSMENT OF CORROSION-FATIGUE DEGRADATION STAGES*. https://doi.org/10.34637/zz27-pa50

Sohn, H. S., & Oh, J. K. (2019). Review of bone graft and bone substitutes with an emphasis on fracture surgeries. In *Biomaterials Research* (Vol. 23, Issue 1). BioMed Central Ltd. https://doi.org/10.1186/s40824-019-0157-y

Szczęsny, G., Kopec, M., & Kowalewski, Z. L. (2025). Toxicity, Irritation, and Allergy of Metal Implants: Historical Perspective and Modern Solutions. In *Coatings* (Vol. 15, Issue 3). Multidisciplinary Digital Publishing Institute (MDPI). https://doi.org/10.3390/coatings15030361

Tabrizian, P., Davis, S., & Su, B. (2024). From bone to nacre - development of biomimetic materials for bone implants: a review. In *Biomaterials Science* (Vol. 12, Issue 22, pp. 5680–5703). Royal Society of Chemistry. https://doi.org/10.1039/d4bm00903g

Tonna, C., & Saliba, L. (2019). *Iron and its alloys for Bone Regeneration Scaffolds-A Review*. https://doi.org/10.7423/XJENZA.2019.1.05

Toosi, S., Javid-Naderi, M. J., Tamayol, A., Ebrahimzadeh, M. H., Yaghoubian, S., & Mousavi Shaegh, S. A. (2023). Additively manufactured porous scaffolds by design for treatment of bone defects. In *Frontiers in Bioengineering and Biotechnology* (Vol. 11). Frontiers Media SA. https://doi.org/10.3389/fbioe.2023.1252636

Wackenrohr, S., Torrent, C. J. J., Herbst, S., Nürnberger, F., Krooss, P., Ebbert, C., Voigt, M., Grundmeier, G., Niendorf, T., & Maier, H. J. (2022). Corrosion fatigue behavior of electron beam melted iron in simulated body fluid. *Npj Materials Degradation*, *6*(1). https://doi.org/10.1038/s41529-022-00226-4

Wang, Y., Zhang, D., & Pan, G. (2023). Investigating the fatigue behavior of 3D-printed bone scaffolds. In *Journal of Materials Science* (Vol. 58, Issue 32, pp. 12929–12953). Springer. https://doi.org/10.1007/s10853-023-08831-7

Wei, Z., Attarilar, S., Ebrahimi, M., & Li, J. (2024). Corrosion and Wear Behavior of Additively Manufactured Metallic Parts in Biomedical Applications. In *Metals* (Vol. 14, Issue 1). Multidisciplinary Digital Publishing Institute (MDPI). https://doi.org/10.3390/met14010096

Witte, F., Fischer, J., Nellesen, J., Vogt, C., Vogt, J., Donath, T., & Beckmann, F. (2010). In vivo corrosion and corrosion protection of magnesium alloy LAE442. *Acta Biomaterialia*, *6*(5), 1792–1799. https://doi.org/10.1016/j.actbio.2009.10.012

Yang, X., Gao, J., Yang, S., Wu, Y., Liu, H., Su, D., & Li, D. (2023). Pore size-mediated macrophage M1 to M2 transition affects osseointegration of 3D-printed PEEK scaffolds. *International Journal of Bioprinting*, *9*(5). https://doi.org/10.18063/ijb.755

Zhang, L., Jiang, B., Zhang, P., Yan, H., Xu, X., Liu, R., Tang, J., & Ren, C. (2023). Methods for fatigue-life estimation: A review of the current status and future trends. In *Nanotechnology and Precision Engineering* (Vol. 6, Issue 2). American Institute of Physics Inc. https://doi.org/10.1063/10.0017255

Zhang, T., Zhou, J., & Shen, J. (2025). Molecular Dynamics Simulation of Low-Cycle Fatigue Behavior of Single/Polycrystalline Iron. *Nanomaterials*, *15*(3). https://doi.org/10.3390/nano15030217

Zhao, D., Han, C., Peng, B., Cheng, T., Fan, J., Yang, L., Chen, L., & Wei, Q. (2022). Corrosion fatigue behavior and anti-fatigue mechanisms of an additively manufactured biodegradable zinc-magnesium gyroid scaffold. *Acta Biomaterialia*, *153*, 614–629. https://doi.org/10.1016/j.actbio.2022.09.047

Zhou, J., Xiong, S., Liu, M., Yang, H., Wei, P., Yi, F., Ouyang, M., Xi, H., Long, Z., Liu, Y., Li, J., Ding, L., & Xiong, L. (2023). Study on the influence of scaffold morphology and structure on osteogenic performance. In *Frontiers in Bioengineering and Biotechnology* (Vol. 11). Frontiers Media S.A. https://doi.org/10.3389/fbioe.2023.1127162

Zhu, J., Zou, S., Mu, Y., Wang, J., & Jin, Y. (2022). Additively Manufactured Scaffolds with Optimized Thickness Based on Triply Periodic Minimal Surface. *Materials*, *15*(20). https://doi.org/10.3390/ma15207084

Appendix I

This appendix presents the individual images of the scaffolds after the fatigue and corrosion-fatigue tests, highlighting the fracture planes identified for each specimen. The dashed lines indicate the predominant fracture orientation, revealing differences in failure modes across stress levels and exposure conditions. For higher applied stresses, the fracture planes tend to be more inclined and consistent between samples, whereas lower stresses lead to greater morphological variability. This set of results complements the information shown in Figure 4.12.

Fatigue - N_2			
013 - 90% σ_Y	**017 – 82% σ_Y**	**018 – 85% σ_Y**	**019 – 85% σ_Y**
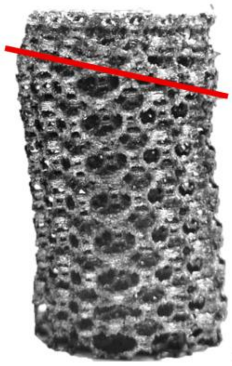	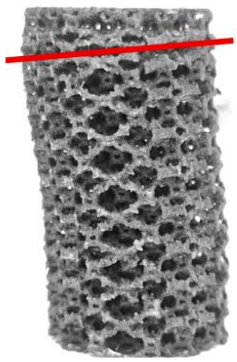	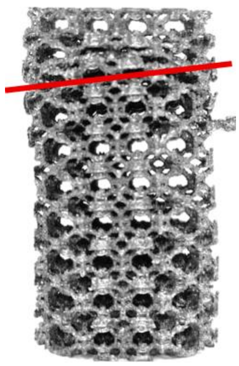	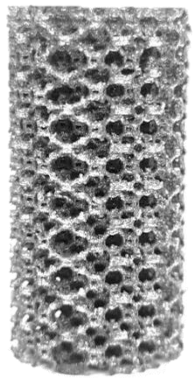
020 - 81% σ_Y	**021 – 76% σ_Y**	**022 – 70% σ_Y**	**023 – 95% σ_Y**
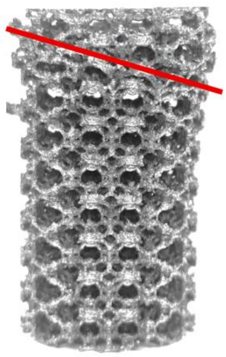	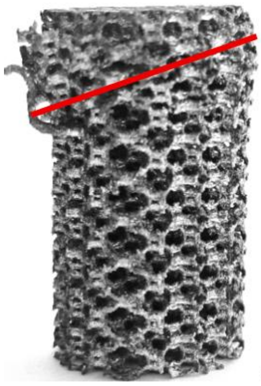	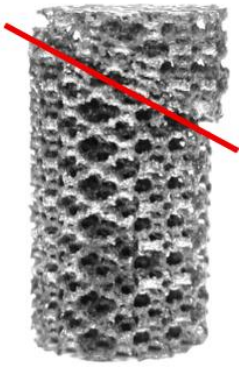	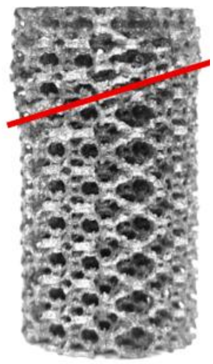

024 – 95% σ_Y
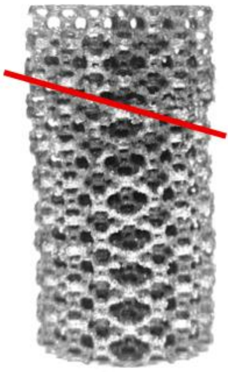

Corrosion - Fatigue - SBF			
051 – 95% σ_Y	052 – 90% σ_Y	053 – 85% σ_Y	054 – 85% σ_Y
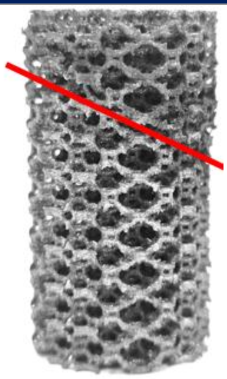	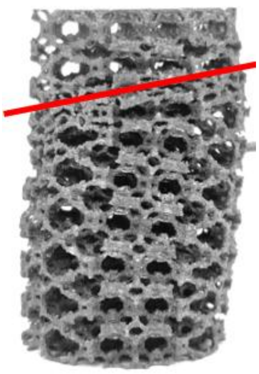	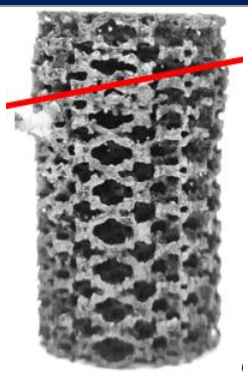	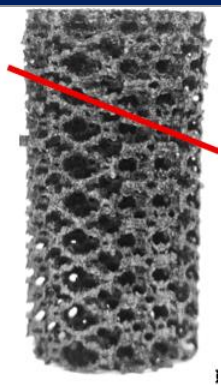
056 – 75% σ_Y	057 – 70% σ_Y	058 – 70% σ_Y	059 – 65% σ_Y
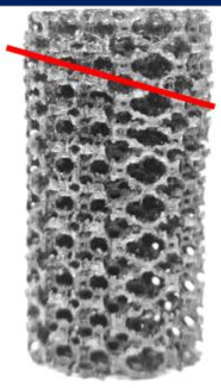	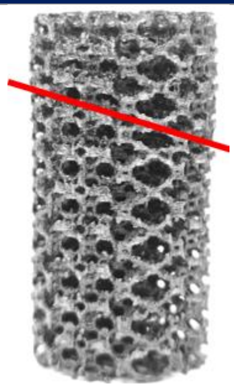	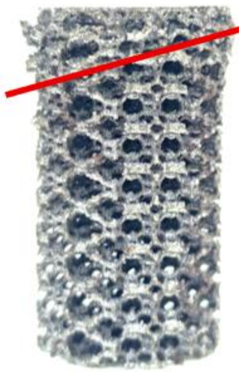	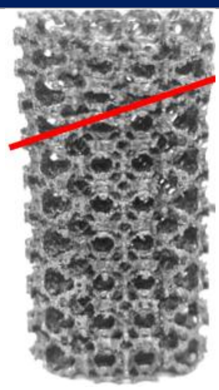

061 – 60% σ_Y	062 – 65% σ_Y	063 – 90% σ_Y	064 – 90% σ_Y
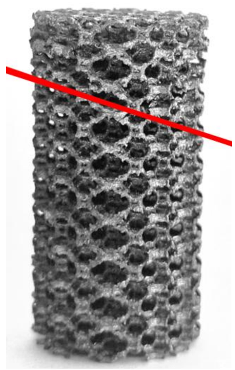	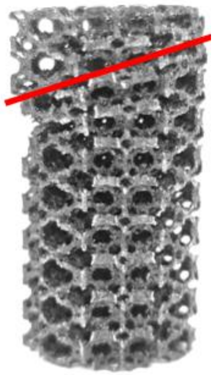	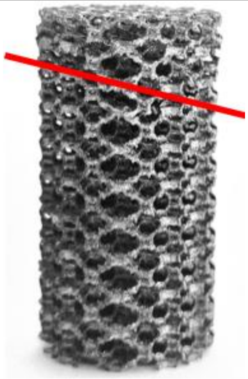	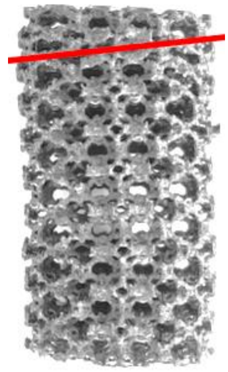
065 – 90% σ_Y